, ,

IMPERIAL COLLEGE LONDON

Department of Mechanical Engineering

Advanced Mechanical Engineering Course

Compliance Regulation of Pneumatic-driven Soft Continuum Robot

Danni Zhou

Supervisor: Ferdinando Rodriguez y Baena

Associate Supervisor: Jialei Shi

Word Count: 15288 words

Word Limit: 18000 words

08/09/2025

A thesis submitted in partial fulfilment of the requirements for the Master of Science Degree of Imperial College London and the Diploma of Membership of Imperial College

Abstract

Due to the inherent compliance and flexibility, soft robots are well-suited for tasks in unstructured environments and human-robot interaction. However, this compliance also limits their payload capacity and control precision, highlighting the need for effective on-demand compliance regulation. This project develops and experimentally validates a model-based real-time control framework for compliance regulation of a pneumatic-driven soft continuum robot. Selective task-space stiffening/softening is achieved with a nonlinear inverse pressure solver built on a quasi-static Cosserat rod model, without auxiliary variable-stiffness mechanisms. The implementation combines MATLAB with an optimised C++ MEX core to support real-time control implementation of more than 1 kHz. Model fidelity is supported by a calibrated pressure–modulus law $E(p)$ embedded in the forward model and verified through trajectory tracking tests on different paths. Directional stiffness regulation experiments confirm monotonic modulation along the principal axes. The framework is demonstrated in three applications—active interaction, trajectory holding under external load, and obstacle avoidance. Overall, the proposed scheme achieves real-time selective softening for safe interaction and stiffening for maintaining trajectories under external loads, enabling practical compliance regulation of soft continuum manipulators.

Acknowledgements

I would like to express my heartfelt gratitude to my supervisor, Prof. Ferdinando Rodriguez y Baena, for his invaluable guidance and continuous encouragement throughout this project. His insightful advice, critical feedback, and rigorous approach have not only shaped the direction and quality of this thesis, but have also greatly enriched my academic experience. I have benefited enormously from his expertise and vision, which will continue to inspire me in my future life.

I am also sincerely grateful to my associate supervisor, Dr. Shi, for his patient and dedicated support at every stage of the project. He provided thoughtful advice on research planning, experimental implementation, data analysis, and writing. His attention to detail and willingness to offer practical help have been of immense value, enabling me to overcome numerous challenges and make steady progress throughout this journey.

I would also like to extend my deepest thanks to my family and friends for their constant support and encouragement. Their understanding, patience, and companionship have given me the strength to persevere during the most challenging moments of my studies.

Contents

List of Figures

List of Tables

1 Introduction

1.1 Background

Robots are programmable machines designed to carry out tasks in the service of human beings. Conventional robots are typically fabricated from rigid materials. They are well suited for structured environments where precision and rigidity are prioritised, but they have limited flexibility and adaptability. Soft robots, instead, are built with soft materials such as hydrogels (Wehner *et al.*, 2016), elastomers (De Pascali *et al.*, 2022). Compared with rigid-body robots, soft robots are safer, more adaptable, and more capable of interacting with humans and other objects in unstructured environments (Rus & Tolley, 2015) due to their compliant properties and have been widely utilised in various fields including industrial production (Zhao *et al.*, 2021), medical rehabilitation (Camp *et al.*, 2021), and agriculture (Navas *et al.*, 2021).

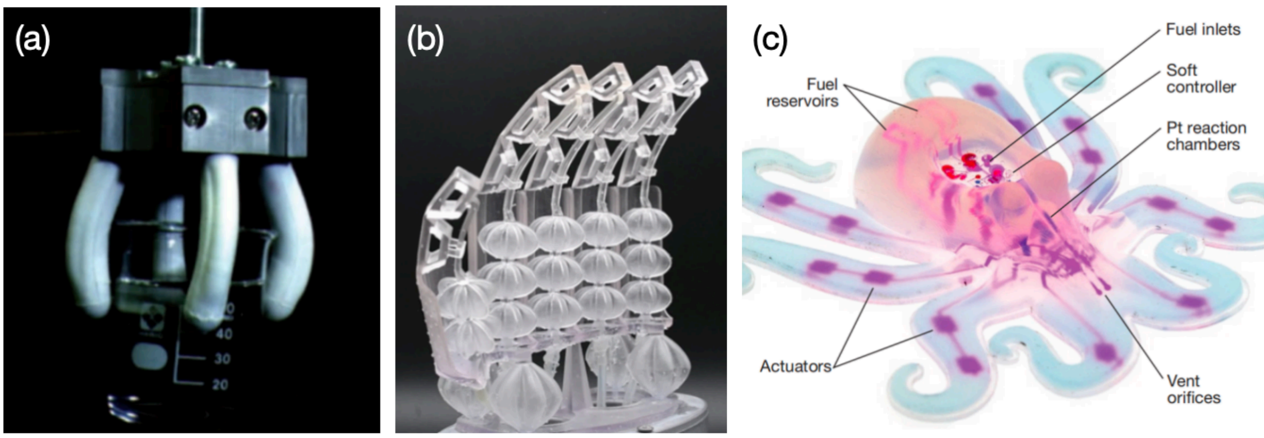

Figure 1: Examples of soft robots: (a) Soft gripper for object manipulation (McMahan et al., 2006) (b) Pleated actuator array enabling bidirectional motion (De Pascali et al., 2022) (c) Untethered octopus-inspired robot with onboard control and actuation (Wehner et al., 2016)

However, the inherent high compliance of soft robots often results in low payload capacity, limiting their adoption in demanding applications such as industrial automation or surgical procedures. Therefore, it is crucial to vary their stiffness properties and achieve effective compliance regulation (Komatsu *et al.*, 2021), i.e., to maintain lower compliance during task execution, while to adopt higher compliance when navigating in environments.

While approaches of incorporating stiffening mechanisms have demonstrated some success, they often come with limitations such as increased complexity, reduced flexibility, and limited tunability. For instance, it might be challenging to embed these variable-stiffness mechanisms in soft manipulators for space-restricted applications, such as minimally invasive surgery (Runciman *et al.*, 2019). In addition, these embedded mechanisms, such as low-melting point alloy (Peters *et al.*, 2019) or jamming structures (Wei *et al.*, 2016a; Yang *et al.*, 2020), usually vary the overall material stiffness of soft robots, which poses challenges when regulating stiffness in desired directions. Model-based approaches offer promising avenues for on-demand stiffness regulation in soft robots, however, they are subject to limitations related to modelling system nonlinearity and computational efficiency (Mahvash & Dupont, 2011). In addition, existing work usually focuses on stiffening control, i.e., to reduce compliance, while stiffness softening control is barely investigated.

In summary, model-based analysis and on-demand control of compliance still remain relatively unexplored and challenging, particularly for soft robots constructed from nonlinear elastomer materials. There is a pressing need for further research to integrate non-linear hyperplasticity into the compliance modelling framework and to realise on-demand compliance control (including both compliance stiffening and softening) in real time, specifically for soft robots without stiffening mechanisms.

1.2 Aim and Objectives

In this project, we investigate how to achieve on-demand compliance regulation of soft robots, encompassing both stiffening and softening, without relying on additional embedded stiffness-varying mechanisms. To address this, we aim to propose a compliance control approach for pneumatic-driven soft continuum robot exhibiting non-linear material hyper-elasticity, where soft robots are capable of maintaining lower compliance during task execution, while possessing higher compliance when navigating in environments.

Specifically, this project has the following objectives:
(1) To model and simulate the compliance properties of a pneumatic-driven soft robot prototype considering the hyper-elasticity of the soft materials.
(2) To propose a model-based compliance control strategy, which is able to achieve both robot softening and stiffening control (along desired directions) of the pneumatic-driven soft continuum robot.
(3) To optimise the numerical computation and achieve real-time control implementation using C++.
(4) To experimentally validate the performance of the approach and demonstrate its potential applications, including human/environment robot interaction and compliance control for trajectory holding and obstacle avoiding.

1.3 Thesis Structure

The structure of this thesis is outlined as follows:

Chapter 1: Introduces the context and motivation for compliance regulation in pneumatically driven soft continuum robots; states the research aim and objectives; and outlines the main contributions and overall structure.

Chapter 2: Reviews compliance analysis and modelling (experimental, FEM, analytical) and compliance control (variable-stiffness mechanisms and model-based approaches), identifying gaps relevant to this work.

Chapter 3: Develops the modelling and control framework: robot description; a Cosserat-rod forward kinematics model with pressure loading and numerical implementation; inverse-kinematics tracking formulated as constrained optimisation; parameter identification; Cartesian configuration-dependent compliance (local/global); and a model-based compliance control strategy with its numerical implementation schemes.

Chapter 4: Presents results: simulation results; identification of the pressure-dependent modulus and cross-trajectory validation; validation of directional compliance regulation; and three applications-external disturbance rejection, trajectory holding under external load, and obstacle avoidance.

Chapter 5: Discusses findings and limitations, including modelling errors and solver sensitivity at higher gains, and reflects on implications for design and control of soft continuum manipulators.

Chapter 6: Concludes the thesis and summarises contributions across modelling, inversion, and compliance control; outlines future work on integrating real-time force feedback, enhancing solver robustness, and refining the $E(p)$ fit for better generalisation.

2 Literature Review

2.1 Compliance Analysis and Modelling

To achieve compliance regulation, it is important to first understand and analyse the stiffness characteristics of soft robots. The stiffness of a soft robot represents the robot's resistance to deformation under applied forces and torques, and the compliance is the inverse of stiffness representing the robot's ability to deform. They can be expressed by the following equations:

$$F = K \cdot \Delta x \tag{1}$$

$$C = K^{-1} \tag{2}$$

K and C are the 6×6 stiffness and compliance matrix, $F = [F_x, F_y, F_z, M_x, M_y, M_z]^T$ is a vector combining forces (F_x, F_y, F_z) and torques (M_x, M_y, M_z), $\Delta x = [\Delta x, \Delta y, \Delta z, \Delta\theta_x, \Delta\theta_y, \Delta\theta_z]^T$ is a vector combining linear ($\Delta x, \Delta y, \Delta z$) and angular ($\Delta\theta_x, \Delta\theta_y, \Delta\theta_z$) displacements. There are three primary methods for stiffness analysis of soft robots: experimental approach, finite element method, and analytical stiffness model.

2.1.1 Experimental Stiffness Analysis

Experimental approach involves performing hands-on experiments to directly observe and measure the stiffness of soft robots. These experiments are conducted under conditions replicating the operational environments of soft robots, where researchers apply controlled forces to the robots in specific directions, record the deformation and calculate the stiffness. The stiffness is defined by the following equation:

$$K = \frac{F}{\Delta x}, \tag{3}$$

K is the stiffness in a specific direction (N/m or equivalent units), F is the applied force (N), and Δx is the measured deformation (mm).

Wei *et al.* (2016b) proposed a simple stiffness testing device. The spine arm was used as a cantilever beam. When load was applied to the end of the robotic spine, the tip displacement was measured from the scaled rule. They analysed the displacement-load relationship and evaluated the stiffness changes under different vacuum pressures. Loeve *et al.* (2010) designed a lift platform where the end of the actuator was hung on a balancer, thus effectively counteracting the influence of gravity. When the lifting platform moved downwards, the pulling force and the platform displacement were recorded by the sensor. Stilli *et al.* (2018) used a camera to record a continuous series of deflection images when external forces were

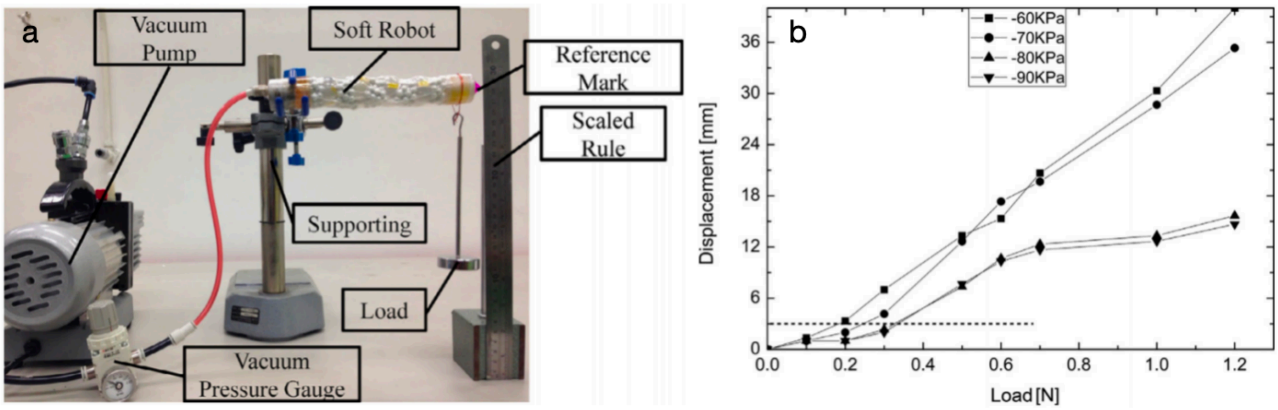

Figure 2: Experimental compliance measurement. (a) Experimental setup, where the load was applied to the end of the robot and the tip displacement was measured from the scaled rule. (b) Displacement-load relationship graph, where the slope represents the compliance (Wei et al., 2016b)

applied to the robot's tip. They converted them to binary images and used Matlab's Image Processing Toolbox to analyse the stiffness property.

Experimental stiffness analysis is accurate and reliable, as it reflects the actual performance of an already fabricated soft robot prototype. It is widely utilised to evaluate the performance of soft robots in a particular direction and to validate robot designs. However, it cannot be used to predict new ones during a design process. Additionally, each robot design requires a unique experimental setup and prototype fabrication, which is time consuming and costly.

2.1.2 Finite Element Method

Finite element method (FEM) is a powerful numerical tool to analyse the stiffness properties of soft robots by simulating the robot's deformation under external loads. The process involves building a geometric model of the soft robot, defining material properties, meshing the model, applying external forces and moments, and using simulation software to compute deformation and derive stiffness properties.

Khalil *et al.* (2024) used Abaqus software to evaluate the influence of four design variables (cross-sectional shape, material, gap shape, and gap size) on the performance of a cable-driven soft manipulator. The results indicated that the triangular cross-sectional shape, Dragon Skin 10 material, trapezoidal gap shape, and 8.87 mm gap size allowed greater flexibility under the same load, making it better suited for delicate material handling tasks. Yang *et al.* (2019) used FEM to verify a virtual trajectory-based kinematic model of eccentric soft bending actuators (ESBAs). They imported a simplified 3-D model of a ESBA in Abaqus software, applied external forces to the end-position of the actuator and found out that under the same initial condition (the actuator exhibited a 90° bending angle when no payload

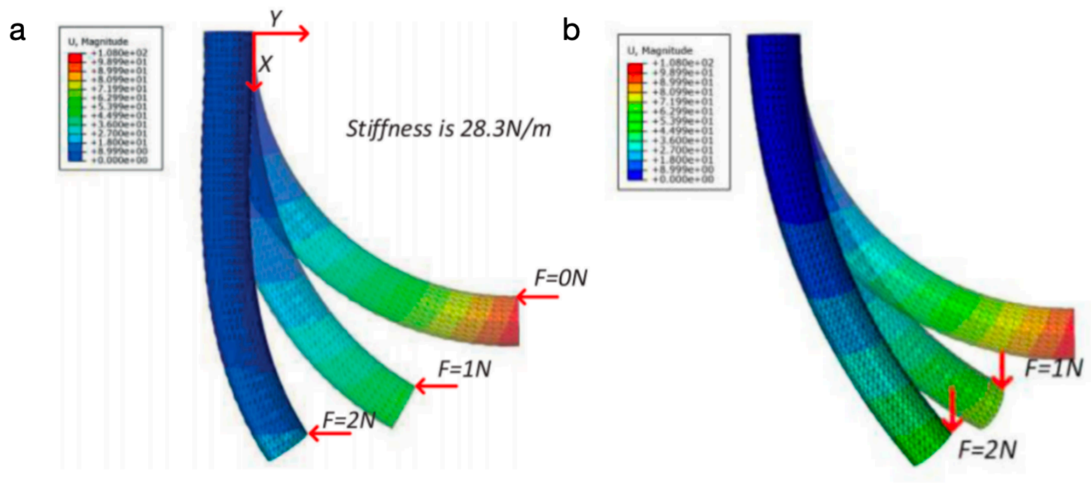

Figure 3: FEM result of a ESBA under (a) horizontal (b) vertical external payload. (Yang et al., 2019)

was applied), the stiffness reduced as the payload increased. They also investigated how geometric parameters (the radius of the chamber and the eccentric distance) affected the stiffness of the actuator.

Finite element method can simulate the performance of soft robots under various conditions. It's widely used to evaluate new designs and helps to optimize the material and geometry of soft robots. However, it's computationally expensive and time-consuming, and requires high modelling accuracy and mesh quality.

2.1.3 Analytical Stiffness Model

While experimental and FEM-based approaches provide valuable insights into the stiffness properties of soft robots, they are primarily used for prototype validation. For a more analytical and generalised understanding of stiffness, stiffness modelling becomes essential. A stiffness model mathematically describes the relationship between applied forces and the resulting deformations of a soft robot under different configurations (a complete specification of the position of all points of the robot (Spong *et al.*, 2020)), enabling the derivation of the Cartesian stiffness matrix, which is fundamental for characterizing stiffness of a soft robot in the operational space. Among the various methods for obtaining stiffness models, two dominant approaches emerge: Jacobian projection and finite difference methods.

Jacobian Projection Method. For rigid robots which have limited numbers of joints, the Cartesian stiffness can be calculated by projecting the stiffness characteristics from the joint space to the task space (Alici & Shirinzadeh, 2005). The relationship between the Cartesian stiffness K_X and the joint stiffness matrix K_θ is described by the following equation:

$$K_X = J^{+T} \left(K_\theta - \frac{\partial J^T}{\partial \theta} F \right) J^+, \tag{4}$$

θ is the displacement of joints, J is the Jacobian matrix, J^+ is the pseudo-inverse Jacobian matrix, and F is the external Force. In contrast, soft robots have continuum bodies without physical joints, the stiffness of which is distributed along the body (Naselli & Mazzolai, 2021). To acquire the stiffness matrix of such a continuum robot, Gravagne & Walker (2002) discretised the continuous backbone into a finite-dimensional system using the finite element method. After that, they calculated the stiffness at the nodal level via interpolation functions and weak-form equations derived from elastic mechanics, and employed Jacobian projection method motivated by equation (4) to map the nodal stiffness matrix to the end-effector stiffness matrix. Della Santina *et al.* (2020) represented the robot as a Piecewise Constant Curvature (PCC) model, assuming that the continuum body is consisted of a series of segments and each segment maintains a constant curvature. Based on material properties and geometry, they derived the stiffness matrix of the segment and employed Jacobian projection to compute task-space stiffness. Huang *et al.* (2022) adopted the Absolute Nodal Coordinate Formulation (ANCF) which used position and position gradients as coordinates to describe the shape of the deformed robot body, then they derived the nodal stiffness matrix from linearised force-displacement relations and projected nodal stiffness to the end-effector space.

Finite Difference Method. Nwafor *et al.* (2023) analysed the stiffness of parallel continuum robots (PCRs) across different plane sections of their workspace and found out that the stiffness varied with respect to both the configuration of the robot and the direction of the applied force. They put forward a finite difference method and calculated the stiffness matrix for each robot configuration within the workspace. Specifically, they measured the change in the tip position resulting from a small incremental change in the applied force, and calculated the stiffness as the finite difference ratio for each axis. The stiffness matrix K can be expressed by the following equation:

$$K \approx \begin{bmatrix} \frac{\Delta F_x}{p_e - p_e^*} & \frac{\Delta F_y}{p_e - p_e^*} & \frac{\Delta F_z}{p_e - p_e^*} \end{bmatrix}, \tag{5}$$

p_e and p_e^* are the tip position with and without force increments of ΔF_x, ΔF_y, and ΔF_z. Rucker & Webster (2011) derived a set of differential equations with boundary conditions based on Cosserat rod approach to describe the shape of a concentric-tube robot. They applied finite difference method to approximate the arc length parametrised compliance matrix by solving the boundary value problem (BVP) iteratively for small perturbations in wrenches. They also put forward a derivative propagation method which significantly improves computational efficiency by propagating derivative information within an initial value problem (IVP), thereby avoiding repeated BVP solutions. The proposed approach is broadly applicable to various continuum robots with different architectures and actuation strategies. Similarly, Black *et al.* (2017) put forward a kinetostatics modelling framework for parallel continuum robots based on Cosserat rod theory, then they introduced small perturbations in actuator forces or external

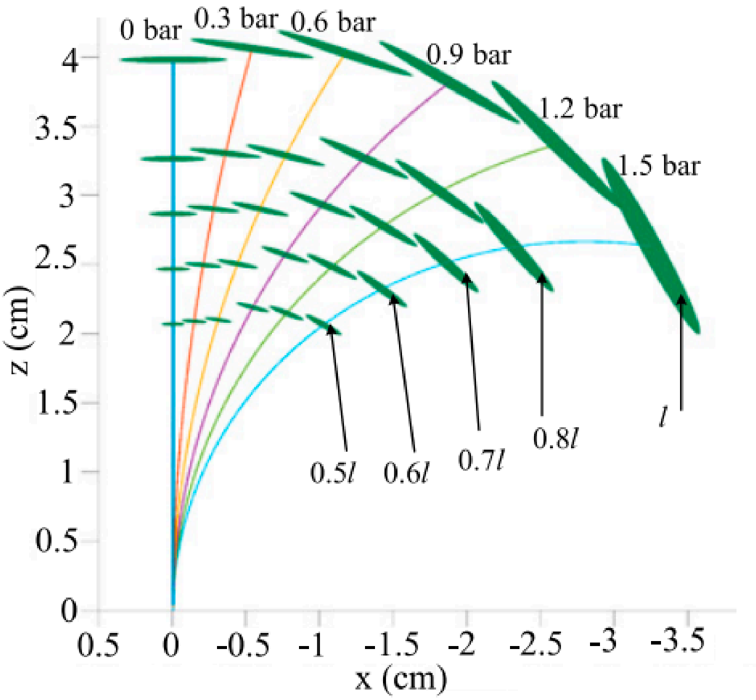

Figure 4: Visualisation of compliance ellipsoids for a manipulator under different configurations. (Shi et al., 2024)

loads and used the resulting deformations to approximate the stiffness matrix.

Based on stiffness matrix K, researchers used stiffness ellipsoid to visualize the stiffness characteristics of soft robots (Gravagne & Walker, 2002). For a given unit displacement vector x, the required force magnitude $\|F\|$ is determined by:

$$\|F\| = \sqrt{x^T K x} \tag{6}$$

The locus of all such forces forms the stiffness ellipsoid, where the axes of the ellipsoid correspond to the principal stiffness directions (eigenvectors of K), the lengths of the axes are proportional to the square roots of the eigenvalues of K. The ellipsoid visually represents stiffness distribution of soft robots, making it easier to understand how the robot interacts with external forces in different directions.

Stiffness model provides clear theoretical insights into the stiffness properties of soft robots, offering a fundamental understanding of how these properties vary with configuration, external forces, and material characteristics. With the help of these model, researchers can achieve a quick stiffness estimation and further implement real-time compliance control in the task space. However, analytical models often face limitations in capturing the nonlinear behaviour of soft materials in complex systems, which requires further investigation.

Table 1: Comparison of experimental approach, finite element method, and analytical stiffness model.

Aspect	Experimental Approach	Finite Element Method	Analytical Stiffness Model
Principle	Direct testing of physical prototypes in a particular direction.	Numerical simulation using computational tools.	Mathematical modelling of stiffness properties.
Accuracy	High, with experimental data.	Moderate, depending on the precision of the model and the quality of the mesh.	Moderate to high, depending on model accuracy.
Scalability	Low, requires multiple prototypes and different experiment set-ups.	High, allows for scaling simulations across multiple designs or configurations.	Moderate to high, applicable across multiple designs or configurations.
Applications	Validation of all kinds of soft robot prototypes.	Performance prediction under various operational conditions and optimization of designs	Configuration-dependent Cartesian stiffness analysis, predictive analysis and real-time control.
Cost	Most expensive, requires fabrication of robots and experimental testing.	Relatively costly, requires specialised software and high-performance computing resources.	The least expensive, only requires basic computational tools.

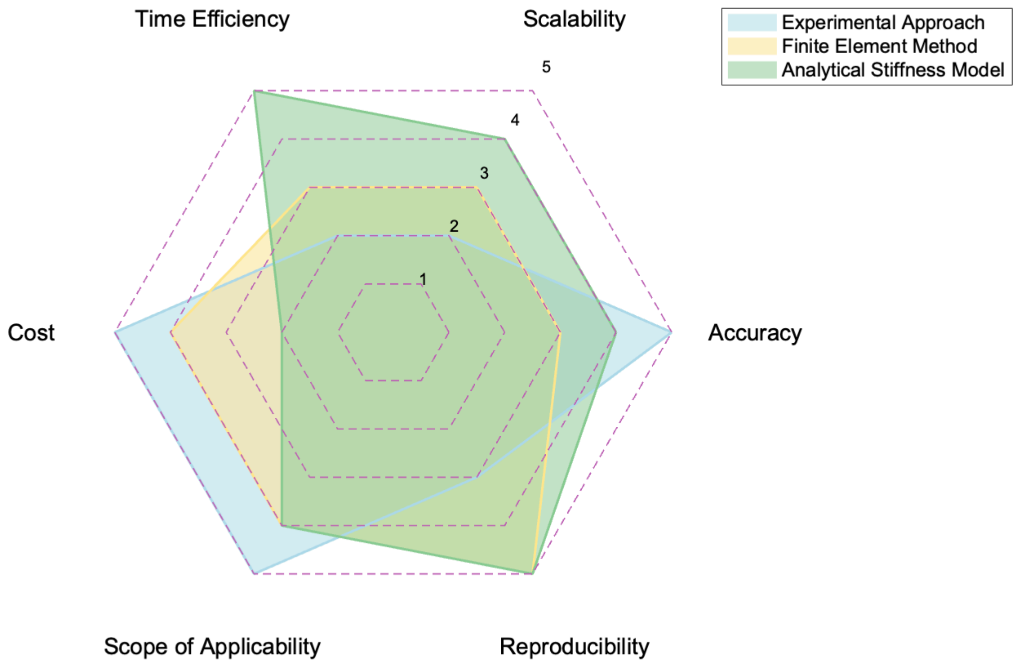

Figure 5: Radar chart comparison of experimental approach, finite element method, and analytical stiffness model.

2.2 Compliance Control

Soft robots exhibit passive compliant behaviours due to the soft materials from which they are constructed. This natural compliance enables them to adapt to external forces, interact safely with delicate objects, and operate in complex and dynamic environments. However, it also introduces challenges in tasks requiring precision, stability, or controlled force. To address

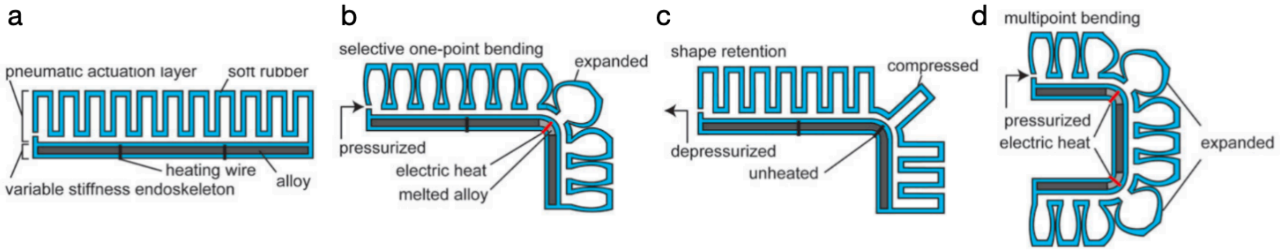

Figure 6: Structure and behaviour of a LMPA-based variable stiffness soft actuator: (a) Structure. (b)-(d) Bending and shape retaining process. (Yoshida et al., 2018)

these challenges, it is essential to achieve active compliance regulation. Current research on compliance control in soft robots can be broadly categorised into two main approaches: variable-stiffness mechanisms and model-based compliance control.

2.2.1 Variable Stiffness Mechanisms

Variable stiffness mechanisms refer to strategies that enable soft robots to modulate their compliance by physically altering their structural or material properties. A number of variable stiffness mechanisms have been explored to to achieve this adaptability, with current studies mainly focusing on rigidity-turnable materials, jamming phenomenon and antagonistic actuation.

Rigidity-Turnable Materials. Rigidity-tunable materials (low-melting-point alloys, shape memory alloys (Liu *et al.*, 2020), etc.) can alter their stiffness in response to external stimuli, such as temperature, chemicals, light, or magnetic fields, and have been widely applied in the design of soft robots to achieve stiffness control. Yoshida *et al.* (2018) proposed a pneumatic bending actuator integrated with a variable stiffness endoskeleton (a low-melting-point alloy layer embedded with metal wires). By applying electric heat through metal wires, the low-melting-point alloy transitioned into a liquid phase and its stiffness decreased. When actuated by air pressure, the actuator bent at the low stiffness point. After removing electric heat, the alloy solidified into a high-stiffness state , and the shape of the bent actuator was retained. However, it was reported that low melting point alloys take long time to change the phase (Peters *et al.*, 2019), making them unsuitable for applications requiring rapid stiffness modulation. Additionally, the performance of these materials can be easily affected by environmental factors like temperature, humidity, etc.

Jamming Phenomenon. The jamming mechanism involves the use of granular or laminar materials, when these materials are compressed or sheared, they jam together and the stiffness of the structure increases. Wei *et al.* (2016a) put forward a variable stiffness gripper based on particle jamming. When no vacuum was applied to the particle chamber, the par-

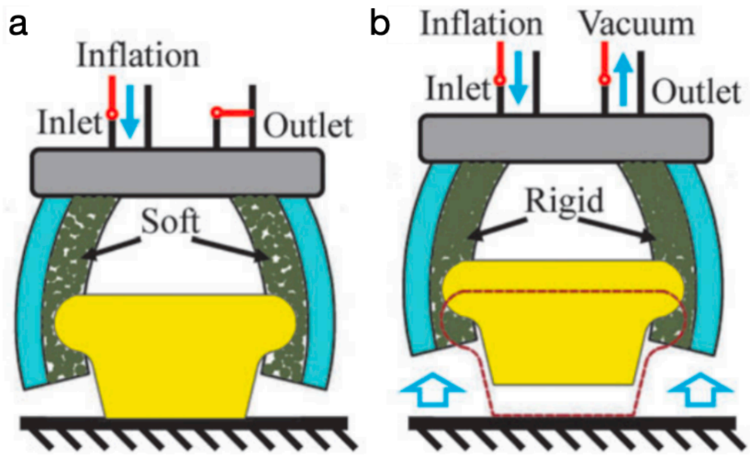

Figure 7: Grasping strategy of a particle jamming-based variable stiffness gripper: (a) Adaption in highly compliant stage without vacuum. (b) Stiffness enhancement in rigid stage through vacuum activation. (Wei et al., 2016a)

ticles were loosely packed, the gripper was highly compliant and can conform to the contact surface. Then a vacuum was applied, the particles were tightly packed and the rigidity of grasping increased. This mechanism can achieve fast and wide-range stiffness change but requires a substantial volume of particles.

Zhu *et al.* (2019) proposed a variable stiffness gripper integrated with a layer jamming unit. Compared with particle jamming-based gripper, it's more lightweight, but the deformability is not that good and therefore can't achieve great adaptivity. Yang *et al.* (2020) designed a novel hybrid jamming-based gripper that was able to transfer between low and high stiffness state for both adaptive grasping and robust holding. Hybrid jamming-based structure takes the advantage of the merits of both layer and particle jamming but requires multiple vacuum inputs which makes the system complicated.

Antagonistic Actuation. The antagonistic mechanism refers to the installation of two or more actuators that act antagonistically on a particular part of robots (Althoefer, 2018). When these actuators are activated, they generate opposing movements or forces, thereby stiffen the whole structure. Babu *et al.* (2019) developed an antagonistic actuator which was composed of two symmetric pneumatic chambers. When only one half was pressurised, the actuator behaved similar to a single pneunet actuator (Ilievski *et al.*, 2011). When both actuators were pressurised, they tended to bend in the opposite direction which resulted in an increase of the actuator stiffness.

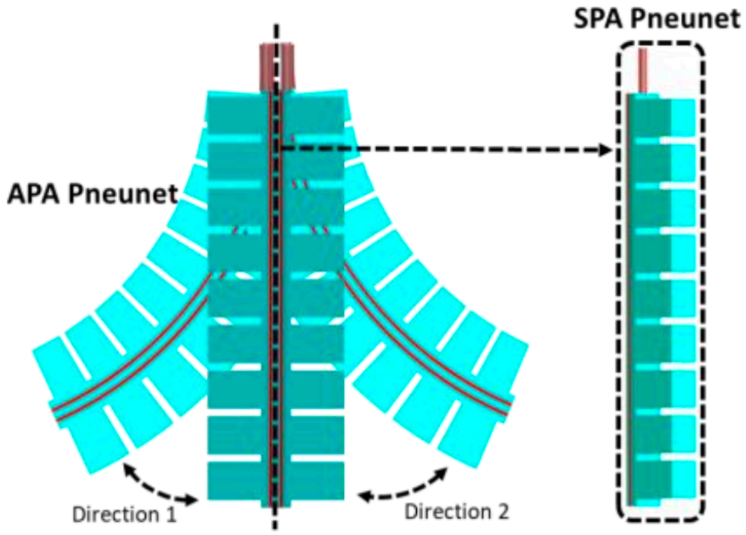

Figure 8: Structure and bending behaviour of an Antagonistic Pneumatic Actuator (APA) which embeds two Single Pneumatic Actuators (SPA). (Babu et al., 2019)

The aforementioned variable-stiffness mechanisms rely on intricate mechanical designs and material selections. However, the relatively large structural size makes it challenging for them to be integrated into soft manipulators, particularly for space-constrained applications such as minimally invasive surgery. Additionally, these mechanisms allow for stiffness modulation at the physical segment level, rather than in the task space (Stella *et al.*, 2023). While for some applications, it's enough to generically alter the physical stiffness, other tasks such as navigating narrow passages, manipulating delicate objects, or assembling components require precise control over the Cartesian stiffness, where certain directions need to be compliant while others maintain rigidity.

2.2.2 Model-Based Compliance Control

As demonstrated in section 2.3, the Cartesian stiffness of soft robots can be analytically described and is configuration dependent. Therefore, by controlling the robot's configuration based on stiffness model, the Cartesian stiffness can be correspondingly modulated.

Based on a coupled kinematic and static force model of a concentric tube robot, Mahvash & Dupont (2011) introduced the first stiffness controller without embedding any stiffening mechanisms. The controller calculated the virtual stiffness force based on the measured tip position, the reference tip position, and a predefined stiffness matrix. This stiffness force represented the desired force response at the robot's tip and was subsequently used to calculate the required deflection, and then the desired undeformed configuration of the robot can be calculated.

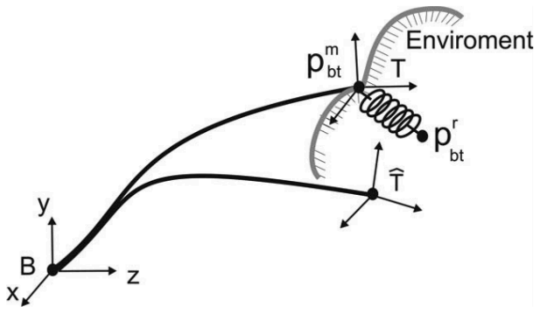

Figure 9: Robot in contact with environment. (Mahvash & Dupont, 2011)

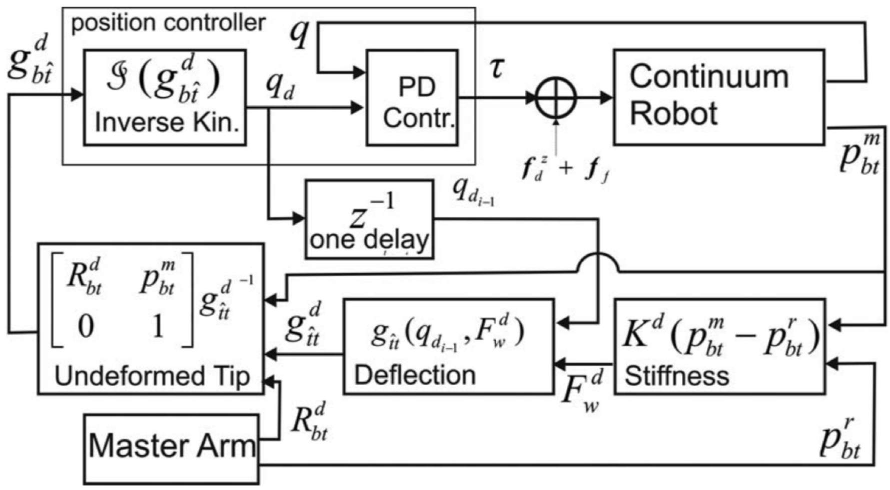

Figure 10: Block diagram of the stiffness controller. (Mahvash & Dupont, 2011)

Figure 14 illustrates how the robot interacts with the environment. When the robot deflects from unloaded configuration $\hat{T}$ to loaded configuration T, the controller implements a virtual linear spring and generates the desired force at the robot's tip, and the desired tip orientation is achieved. Figure 10 provides a detailed illustration of the control process. K_d is the desired stiffness matrix, p^r_{bt} and p^m_{bt} are the reference and measured tip position, F^d_w is the desired force, $g^d_{t\hat{t}}$ is the tip displacement under the applied load, and $g^d_{b\hat{t}}$ is the tip configuration without load.

Similarly, Aloi *et al.* (2018) designed a closed-loop stiffness control approach for a parallel continuum robot based on a force-sensing kinetostatic model formulation (the kinetostatic model is based on Cosserat rods). The control law employed an integral control strategy to adjust the target position based on the desired stiffness and the measured tip force. This approach is broadly applicable to any manipulator that has a model with the same inputs and outputs. Lai *et al.* (2021) put forward a stiffness controller for a dual-segment tendon-driven soft robot utilizing depth vision. They employed the eye-to-hand RGB-D visual tracking technology to detect the spatial deviation of the end-effector resulting from an axial payload. The

Table 2: Comparison of variable stiffness mechanisms and model-based compliance control.

Aspect	**Variable Stiffness Mechanisms**	**Model-Based Compliance Control**
Implementation	Relies on physical/material properties and simple control strategies.	Requires analytical stiffness models and advanced algorithms.
Stiffness Adjustment	Often limited to pre-defined states, modulate stiffness at physical segment level.	Capable of closed-loop control based on real-time feedback, modulate stiffness in the task space.
Adaptability	Restricted to tasks or environments that align with the pre-designed mechanical properties.	Highly adaptive to changing tasks and environments.
Applications	Suitable for relatively simple tasks (e.g., flexible grippers, rehabilitation devices).	Ideal for high-precision tasks (e.g., industrial automation, surgical robots).

spatial deriviation was considered as the feedback of the controller and the needed compensation tendon actuation can be computed to adjust the stiffness of the manipulator. For a novel tendon-driven soft manipulator equipped with variable-stiffness segments and capable of three dimensional movement, Stella *et al.* (2023) proposed an analytical model that linked the Cartesian stiffness at the end-effector to the physical stiffness and the robot's posture. They then developed an algorithm to control the Cartesian stiffness of the robot by co-modulating posture and physical stiffness. The performance of this model-based compliance controlling method was proven to exceed the performance achievable with variable stiffness mechanisms only. However, this system lacked a feedback mechanism, relying entirely on pre-computed result, and was therefore unable to dynamically adjust to disturbances during operation.

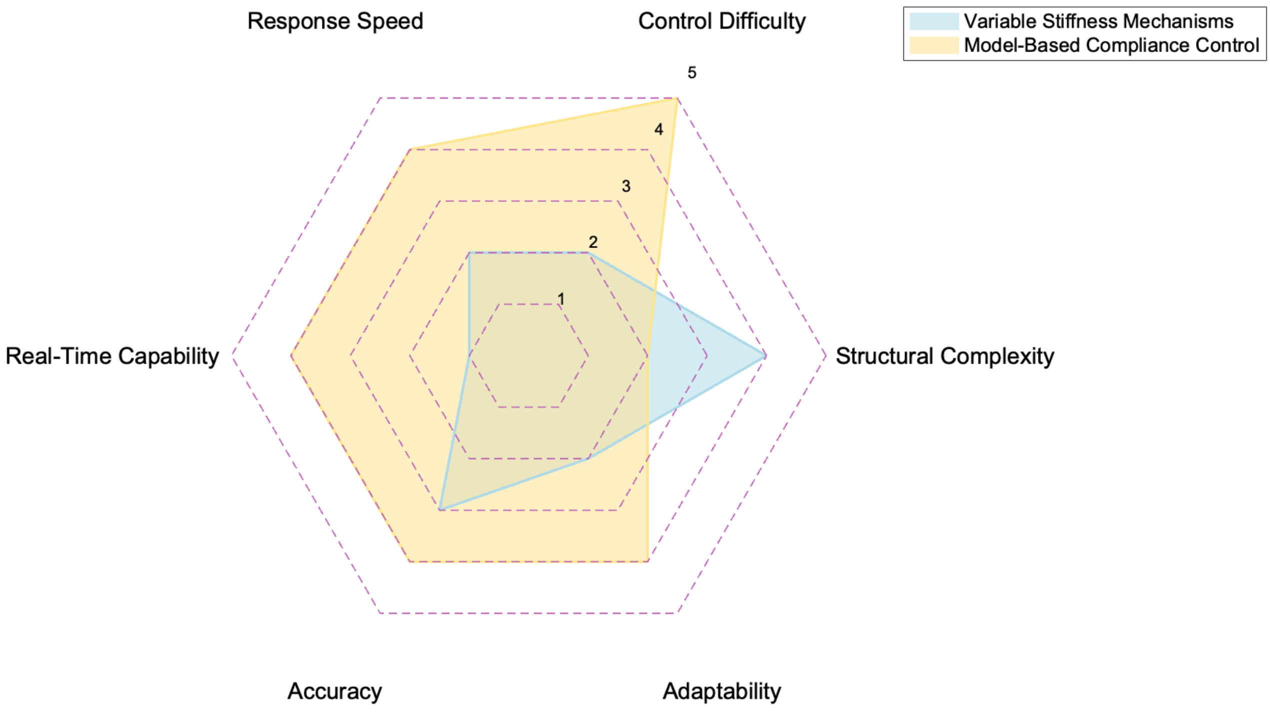

Figure 11: Radar chart comparison of variable stiffness mechanisms and model-based compliance control.

In summary, model-based compliance control minimises reliance on physical stiffening mechanisms, reducing robot weight and complexity while enhancing adaptability. It allows for precise and real- time compliance control in task space, and can be applied into complex tasks such as minimal invasive surgery. However, challenges such as reliance on accurate models and high computational demands must be addressed.

3 Methodology

This chapter presents the complete modelling and control framework developed in this project. The proposed approach integrates a Cosserat rod-based forward kinematics model, an inverse solver for pressure computation, compliance analysis, and a model-based compliance control strategy. The chapter first introduces the soft robot prototype and actuation principles, then describes the forward kinematics model, inverse solver, and parameter identification procedure. It concludes with the compliance analysis framework and the proposed compliance control strategy, together with their numerical implementations. All computational algorithms were implemented in MATLAB and optimised in C++ for real-time performance, with seamless integration via MEX functions.

3.1 Robot Description

3.1.1 Robot Prototype

The soft robot used in this project is pneumatically actuated and composed of fully reinforced silicone chambers arranged symmetrically around a central lumen. The robot has an overall length of 115 mm and an external radius of 11.5 mm. The central lumen with a radius of 5 mm provides space for instrumentation such as sensors or medical tools. Surrounding the lumen are nine actuation chambers, grouped into three pairs and evenly distributed at 120° intervals around the circumference. Each chamber has an internal radius of 2.25 mm and is positioned 8.25 mm from the central axis.

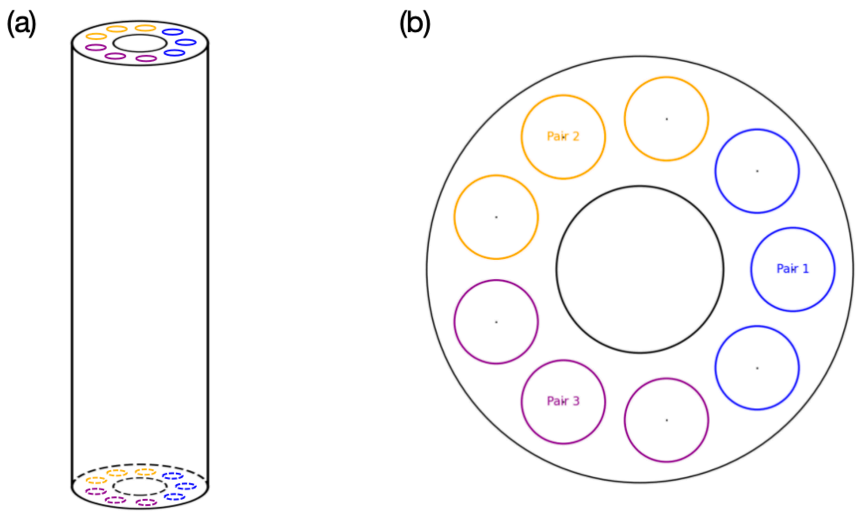

Figure 12: Geometric design of the soft robot prototype: (a) Overall structure (b) Cross-sectional layout

3.1.2 Working Principle

The soft robot is actuated pneumatically by inflating internal chambers with controlled pressures. By controlling the pressure in each chamber pair, asymmetric force distributions are generated along the body of the robot, resulting in targeted shape deformations. When a single pair of chambers is pressurised, the soft robot bends toward the opposite direction of the actuated chambers, whereas multi-pair chamber pressurisation produces omnidirectional bending and elongation.

3.2 Forward Kinematics Model

3.2.1 Cosserat Rod Theory

The forward kinematics model of the soft robot is built upon Cosserat rod theory (Rucker & Webster, 2011). According to this theory, the robot backbone can then be modelled as a continuous rod, the internal and external force and moment distributions along the rod (on the ith segment) are shown in Figure 13.

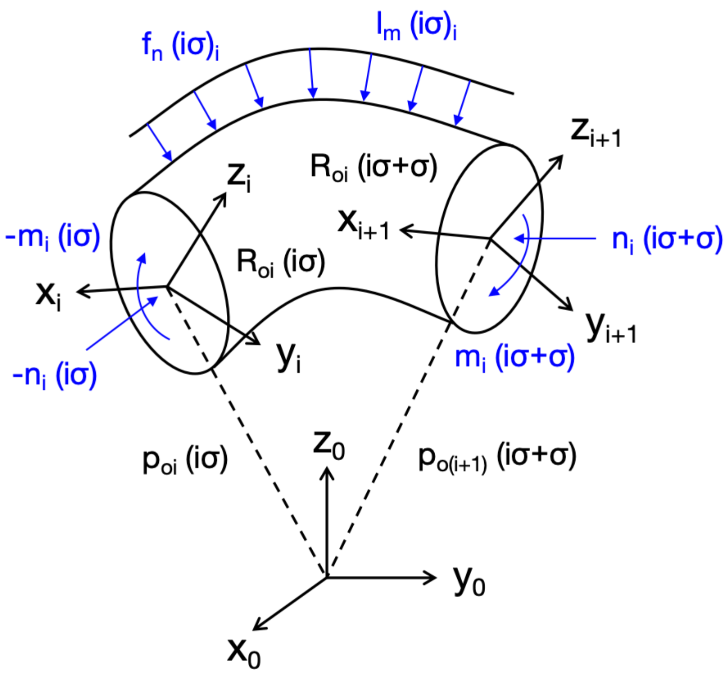

Figure 13: Forces, moments, and local frames acting on the ith Cosserat rod segment

Based on this, the static Cosserat rod model can be described by the following set of ordinary differential equations (ODEs):

$$\begin{cases} (p_{oi}(s))_s = R_{oi}(s)v_i^b(s), \\ (R_{oi}(s))_s = R_{oi}(s)\hat{u}_i^b(s), \\ (n_i(s))_s = -f_e(s)_i, \\ (m_i(s))_s = -p_{oi}(s)_s \times n_i(s) - l_e(s)_i, \end{cases} \tag{7}$$

where $p_{oi}(s)$ is the position vector along the rod, $R_{oi}(s)$ is the rotation matrix describing orientation along the rod, $v_i^b(s)$ and $u_i^b(s)$ are linear strain and curvature vectors in the local frame, $n_i(s)$ and $m_i(s)$ are internal force and moment vectors, and $f_e(s)_i$ and $l_e(s)_i$ are external distributed force and moment vectors.

3.2.2 Incorporation of Pneumatic Pressure

Considering pneumatic pressures in chambers, the model equations become:

$$\begin{cases} (p_{oi}(s))_s = R_{oi}(s)v_i^b(s), \\ (R_{oi}(s))_s = R_{oi}(s)\hat{u}_i^b(s), \\ (n_i(s))_s = -f_e(s)_i + f_P(s)_i, \\ (m_i(s))_s = -p_{oi}(s)_s \times n_i(s) - l_e(s)_i + l_P(s)_i \end{cases} \tag{8}$$

Pressure-induced force and moment $f_P(s)_i$ and $l_P(s)_i$ can be expressed as follows:

$$\begin{cases} f_P(s)_i = \sum_{k=1}^{9} P_k A_P R_{oi}(s) e_3, \\ l_P(s)_i = \sum_{k=1}^{9} P_k A_P R_{oi}(s) \left[\left(v_i^b(s) + u_i^b(s) \times k^d \right) \times e_3 \right] \end{cases} \tag{9}$$

where P_k is the pneumatic pressure, A_P is the cross-sectional area of each chamber, $e_3 = [0, 0, 1]^T$ is the unit vector along the backbone, and k^d is the vector representing the position of each chamber centre.

3.2.3 Numerical Implementation

This section presents the numerical implementation of the forward kinematics based on the Cosserat rod model. The main objective is to determine the robot's spatial configuration by integrating the governing ODEs along its arc length $s \in [0, L]$.

The configuration of the soft robot is described by the state vector:

$$y(s) = \begin{bmatrix} p(s) \\ \text{vec}(R(s)) \\ n(s) \\ m(s) \\ \text{vec}(C(s)) \end{bmatrix}, \tag{10}$$

where $p(s)$ is the position vector, $R(s)$ is the rotation matrix, $n(s)$ and $m(s)$ are the internal force and moment vectors, and $C(s)$ is the compliance matrix.
The governing equations for our soft robot are as follows:

$$\begin{cases} p'(s) = R(s)\, v(s), \\ R'(s) = R(s)\, \hat{u}(s), \\ n'(s) = -f_p(s) - \rho A g, \\ m'(s) = -p'(s) \times n(s) + l_p(s), \end{cases} \tag{11}$$

Since the base values of internal force (n_0) and moment (m_0) are unknown, a shooting method is adopted. An initial guess is iteratively refined to ensure that the solution satisfies boundary conditions at $s = L$. The numerical integration is performed using a fourth-order Runge-Kutta (RK4) scheme, which solves the ODEs over discrete steps.
The following pseudocode summarizes the overall numerical implementation.

Algorithm 1 ForwardKinematics(p1, p2, p3)

1: Input: Pressures p_1, p_2, p_3
2: Initialise system parameters and base conditions:

$$\text{Params} \leftarrow \text{InitialiseParameters}(p_1, p_2, p_3)$$

3: Form the base state:

$$y_0^{\text{base}} \leftarrow [p_0, R_0, n_0^{\text{guess}}, m_0^{\text{guess}}, C_0]$$

4: Solve for the unknown base values using the shooting method:

$$G_{\text{sol}} \leftarrow \text{SolveNonlinearSystem}(\text{ShootingResidual}, \text{initial\_guess} = [0, 0, 0, 0, 0, 0])$$

5: Construct the complete initial state:

$$y_0 \leftarrow \text{ConstructState}(p_0, R_0, G_{\text{sol}}, C_0)$$

6: Numerically integrate the ODE from $s = 0$ to $s = L$:

$$y_{\text{final}} \leftarrow \text{RK4Integrator}(\text{ODEfunc}, y_0, s_{\text{start}} = 0, s_{\text{end}} = L)$$

7: Return the end-effector configuration:

$$\text{ExtractEndEffectorState}(y_{\text{final}})$$

Algorithm 2 ShootingResidual(G)

Construct the state with guessed base values:

$$y_0 \leftarrow \text{ConstructState}(p_0, R_0, G, C_0)$$

Integrate the ODE system:

$$y_L \leftarrow \text{RK4Integrator}(\text{ODEfunc}, y_0, s_{\text{start}} = 0, s_{\text{end}} = L)$$

Compute the residual between computed and desired end states:

$$E \leftarrow \text{ComputeResidual}(y_L, \text{DesiredEndState})$$

Return E

Algorithm 3 RK4Integrator(ODEfunc, y_0, s_{start}, s_{end})

Set step size:

$$h \leftarrow \frac{s_{\text{end}} - s_{\text{start}}}{N}$$

Initialize:

$$y \leftarrow y_0, \quad s \leftarrow s_{\text{start}}$$

for $i = 1$ **to** N **do**

  $k_1 \leftarrow \text{ODEfunc}(s, y)$

  $k_2 \leftarrow \text{ODEfunc}\left(s + \frac{h}{2},\ y + \frac{h}{2}k_1\right)$

  $k_3 \leftarrow \text{ODEfunc}\left(s + \frac{h}{2},\ y + \frac{h}{2}k_2\right)$

  $k_4 \leftarrow \text{ODEfunc}(s + h,\ y + hk_3)$

  Update:

$$y \leftarrow y + \frac{h}{6}(k_1 + 2k_2 + 2k_3 + k_4)$$

  $s \leftarrow s + h$

end for

Return y

3.3 Inverse Kinematics Tracking Control

3.3.1 Theoretical Basis

To achieve trajectory tracking for a pneumatic-driven soft continuum robot, the inverse kinematics (IK) problem is formulated as a constrained nonlinear optimization. The objective is to compute a set of chamber pressures $P = [p_1, p_2, p_3] \in \mathbb{R}^n$, such that the robot tip closely follows a desired pose in task space.

Given a desired target pose (p_d, R_d) at the robot tip, the IK problem aims to minimize a cost function composed of residual statics and pose tracking errors:

$$\min \|e_n\|^2 + \|e_m\|^2 + \|e_p\|^2 + \|e_R\|^2 \tag{12}$$

where $e_n = n(L) - n_{\text{desired}}$ is the residual internal force, $e_m = m(L) - m_{\text{desired}}$ is the residual internal moment, $e_p = \|p_r - p_d\|_2$ is the tip position error, and $e_R = \left(R_r^T R_d - R_d^T R_r\right)^\vee$ is the orientation error.

This optimization is solved iteratively using a shooting method, which integrates the Cosserat rod ODEs to compute the forward kinematics, and a nonlinear solver (e.g., Levenberg–Marquardt or MATLAB's fsolve) to update the pressure vector P. The base internal force and moment are treated as unknowns and initialised with guesses, which are refined until convergence.

In the single-segment implementation, the tip pose is computed by integrating the Cosserat rod equations under a given pressure set. In the two-segment case, the procedure involves sequential integration of two Cosserat rod models, connected by a rigid interface where continuity of position, orientation, force, and moment is enforced.

3.3.2 Numerical Implementation

The overall control process is summarised in the following pseudocode. The algorithm computes the optimal actuation pressures required to match the desired end pose.

Algorithm 4 Inverse Kinematics Tracking

Require: Desired tip pose: p_d, R_d; initial pressure guess P_0; forward kinematics solver
Ensure: Optimised pressure vector P to minimize tracking errors

1: Initialise pressure guess: $P \leftarrow P_0$
2: **Repeat**
3: Compute current tip pose (p_r, R_r) under pressure P via forward kinematics
4: Compute tracking errors:

$$e_p = \|p_r - p_d\|_2, \quad e_R = \left(R_r^\top R_d - R_d^\top R_r\right)^\vee, \quad e_n = n(L) - n_{\text{desired}}, \quad e_m = m(L) - m_{\text{desired}}$$

5: Evaluate static residuals from Cosserat rod model:
6: Define cost function:

$$J(P) = \|e_n\|^2 + \|e_m\|^2 + \|e_p\|^2 + \|e_R\|^2$$

7: Update P using nonlinear optimization (e.g., Levenberg–Marquardt)
8: **Until** convergence or maximum iterations reached
9: **Return** optimised pressure P

3.4 Compliance Modelling

Accurate modelling of compliance is essential to fully describe how a pneumatic-driven soft robot deforms under internal actuation and external loading. In this project, the compliance is analysed using the Cosserat rod framework, extended to include pneumatic pressure effects, and numerically integrated simultaneously with the forward kinematics. This section presents the theoretical foundation and computational steps used to derive and evaluate the compliance matrices of the soft robot.

3.4.1 Compliance Matrix in Cosserat Rod Theory

As illustrated previously in Section 2.2.1, a soft continuum robot can be discretised into small segments, each following the Cosserat rod equations. In the general 6-degree-of-freedom (6-DOF) representations, compliance is described by a 6×6 matrix C, which maps applied forces and moments $W \in \mathbb{R}^6$ to the resulting infinitesimal twist $T \in \mathbb{R}^6$:

$$T = CW \quad \Longleftrightarrow \quad W = KT, \quad \text{where } C = K^{-1}. \tag{13}$$

Here, T consists of translational and rotational components $(\delta p,\, \delta\theta)$, and W represents the corresponding force and torque $(\delta f,\, \delta m)$.

3.4.2 Local and Global Compliance

To thoroughly characterize compliance in the Cosserat rod-based soft robot, it is essential to distinguish between local and global measures.

For each infinitesimal rod segment, the compliance is represented by a local compliance density matrix c_0. It's often diagonal and can be expressed as follows:

$$c_0 = \text{diag}\left[(GA)^{-1},\ (GA)^{-1},\ (EA)^{-1},\ (EI)^{-1},\ (EI)^{-1},\ (GJ)^{-1}\right]. \tag{14}$$

where G is the shear modulus, E is the Young's modulus, A is the cross-sectional area of the robot, I is the second moment of area, and J is the polar moment of inertia.

The compliance density c_0 for each rod segment is transformed to a consistent global frame, then, by numerically integrating the transformed compliance density from $s = 0$ to $s = L$, we obtain a final 6×6 global compliance matrix at the robot tip:

$$g_{\text{compliance}} \in \mathbb{R}^{6\times 6}. \tag{15}$$

For practical applications, it is often beneficial to represent compliance in the robot's own reference frame. Therefore, we need an adjoint operation to transform the global compliance matrix back into the body-frame compliance matrix:

$$b_{\text{compliance}} = \text{Adj}(R,p)^T\ g_{\text{compliance}}\ \text{Adj}(R,p). \tag{16}$$

where R and p denote the orientation and position at the rod tip, and Adj(R, p) is the 6×6 adjoint transformation matrix. This results in a body-frame compliance matrix $b_{compliance}$ that characterizes the local compliance precisely at the tip's reference coordinate system.

The compliance ellipsoid provides a geometric interpretation of the robot's local compliance at the tip (Gravagne & Walker, 2002). It illustrates how the robot deforms under unit external forces in different directions, and is directly derived from the translational part of the body-frame compliance matrix.
Given the local compliance matrix $C \in \mathbb{R}^{6\times6}$, the translational compliance ellipsoid is defined as:

$$\mathcal{E} = \left\{ \boldsymbol{x} \in \mathbb{R}^3 \,\middle|\, \boldsymbol{x}^\mathsf{T} C_{\mathrm{ff}}^{-1} \boldsymbol{x} = 1 \right\} \tag{17}$$

where $C_{\mathrm{ff}} \in \mathbb{R}^{3\times3}$ is the translational sub-matrix of C, mapping forces to linear displacements. The ellipsoid's axes are aligned with the eigenvectors of C_{ff}, and their lengths are proportional to the square roots of the corresponding eigenvalues. A longer axis indicates higher compliance in that direction, while a shorter one implies increased stiffness.

3.4.3 Numerical Implementation

As discussed above, the compliance analysis is numerically realised through simultaneous integration with the Cosserat rod forward kinematics. The pseudocode below summarizes the detailed numerical steps for computing and transforming the compliance matrix.

Algorithm 5 Compliance Matrix Integration and Transformation

1: Initialize local compliance density matrix:

$$c_0 = \mathrm{diag}\left[(GA)^{-1}, (GA)^{-1}, (EA)^{-1}, (EI)^{-1}, (EI)^{-1}, (GJ)^{-1}\right]$$

2: Initialize state vector:

$$y(0) = [p,\ \mathrm{reshape}(R, 9),\ n,\ m,\ \mathrm{reshape}(C, 36)]$$

3: **for** $s = 0$ to $s = L$ **do**
4: Compute $\frac{dp}{ds}$ and $\frac{dR}{ds}$ via Cosserat rod equations
5: Compute $\frac{dn}{ds}$ and $\frac{dm}{ds}$ including pneumatic actuation effects
6: Update compliance matrix derivative $\frac{dC}{ds}$ using c_0
7: Formulate the complete state derivative vector $\frac{dy}{ds}$
8: Integrate state one step forward using an ODE solver (e.g., RK4)
9: **end for**

Algorithm 5 Compliance Matrix Integration and Transformation (cont.)

10: At $s = L$:

11: Extract global compliance matrix at robot tip:

$$g_{\text{compliance}} = \text{reshape}(y_{\text{end}}(19:54), 6, 6)$$

12: Transform global compliance matrix into body frame:

$$b_{\text{compliance}} = \text{Adj}(R, p)^T \cdot g_{\text{compliance}} \cdot \text{Adj}(R, p)$$

13: **Return** $g_{\text{compliance}}$, $b_{\text{compliance}}$

3.5 Compliance Control

3.5.1 Control Strategy

In tasks involving physical interaction with unknown environments, it is desirable for the soft continuum manipulator to regulate its endpoint stiffness to ensure both safety and accuracy. Instead of relying solely on position control or force feedback, the proposed approach utilises a model-based strategy that integrates the Cosserat rod formulation with a virtual spring model. By defining a desired Cartesian stiffness K_d at the manipulator tip, the internal chamber pressures P are adjusted such that the actual compliance matches the desired behaviour.

To achieve this, the endpoint is treated as connected to the reference position p_r via a virtual spring. The desired restoring force is

$$F_d = K_d\left(p_m - p_r\right). \tag{18}$$

where $p_m \in \mathbb{R}^3$ is the measured endpoint position from the Aurora electromagnetic tracking system, and $K_d = \text{diag}(k_x, k_y, k_z)$ specifies the commanded Cartesian stiffness along the x, y, z axes. In experiments, stiffness regulation can be applied selectively to one or more directions, depending on task requirements.

Given the desired force F_d and the current chamber pressures P, the Cosserat rod model is used to predict the resulting tip deflection. Linearising the equilibrium equations around the current configuration yields the local compliance matrix $C(P) \in \mathbb{R}^{6\times 6}$, relating a small applied wrench $W = [F^\top\ M^\top]^\top$ to the incremental twist $\delta\xi = [\delta p^\top\ \delta\theta^\top]^\top$:

$$\delta\xi = C(P)\,W. \tag{19}$$

For a pure force input, the predicted translational deformation at the tip is extracted as

$$\Delta p = \delta p = \begin{bmatrix} I_{3\times 3} & 0_{3\times 3} \end{bmatrix} \delta\xi. \tag{20}$$

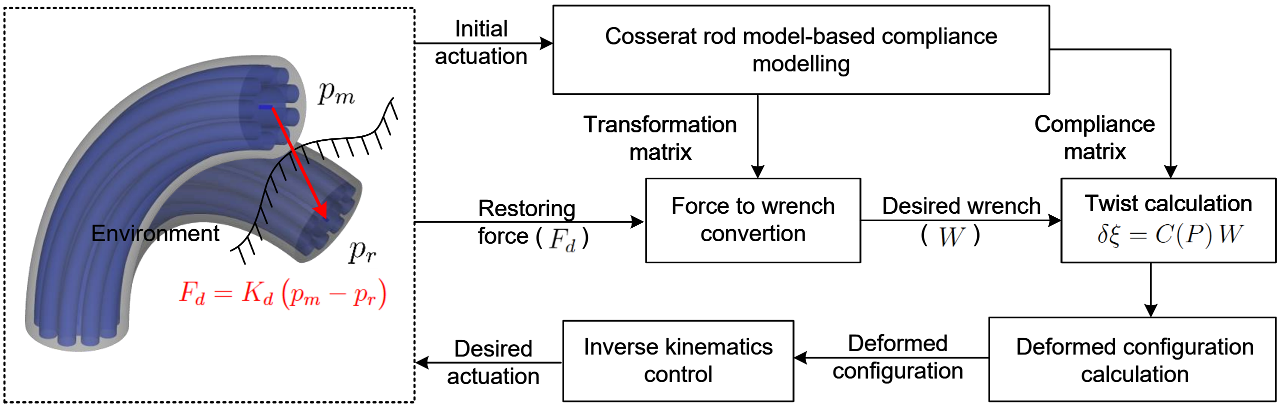

Figure 14: Structure of the model-based compliance control framework.

This prediction is implemented in `FYP_Deform_New`, which integrates the Cosserat rod static equilibrium using a shooting method. Given chamber pressures and desired forces, it returns Δp, which is then used for feedforward compensation in the compliance loop.

After computing Δp, the control objective is to compensate this deformation so the manipulator realises the desired endpoint stiffness. The target tip position is updated by subtracting the predicted deformation from the reference:

$$p^* = p_r - \Delta p, \tag{21}$$

where Δp is obtained from (20). This feedforward compensation helps maintain the commanded stiffness behaviour under unknown external loading.

To achieve p^*, the inverse kinematics solver `FYP_Tip_Inverse_mex` computes the optimal chamber pressures P^*:

$$P^* = \arg\min_P \left\| p(P) - p^* \right\|^2, \tag{22}$$

posed as a boundary-value shooting problem. In practice, the solver is warm-started with the last estimate to improve convergence and numerical robustness.

The computed P^* are sent to the pneumatic controller, the new endpoint p_m is measured by Aurora, and the procedure repeats in the next cycle. This real-time loop combines model-based feedforward with tip-position feedback for stiffness regulation in Cartesian space.

3.5.2 Numerical Implementation

The compliance controller integrates the forward model, the compliance prediction, and the inverse pressure solver. The pseudocode below summarises the strategy.

Algorithm 6 Model-based Compliance Control

Input: desired stiffness K_d, reference tip position p_r
Output: optimal chamber pressures P^*
Initialise pressures $P \leftarrow 0$
Measure initial tip position p_m (Aurora)
while control loop is active **do**
    Acquire current p_m (Aurora)
    Compute desired restoring force: $F_d \leftarrow K_d\,(p_m - p_r)$
    Predict tip deformation $\Delta p \leftarrow \texttt{FYP\_Deform}(P, F_d)$
    Update target: $p^* \leftarrow p_r - \Delta p$
    Solve for pressures: $P^* \leftarrow \texttt{FYP\_Tip\_Inverse}(p^*)$
    Apply P^* to pneumatic controller; set $P \leftarrow P^*$
end while

Algorithm 7 Computation of Tip Deformation with `FYP_Deform`

Input: chamber pressures P, desired endpoint force $F_d \in \mathbb{R}^3$
Output: predicted tip deformation $\Delta p \in \mathbb{R}^3$
Initialise Cosserat state at $s = 0$: $y(0) = [p_0, R_0, n_0, m_0]$
Set material/geometric data: $A, I, J, \rho, E(P)$
Shooting: find base wrench $G^* = [n_0^\top \ m_0^\top]^\top$ such that

$$E(G,P) = \begin{bmatrix} n(L;G,P) - F_{\text{tip}} \\ m(L;G,P) - M_{\text{tip}} \end{bmatrix} = 0, \quad F_{\text{tip}} = F_d, \ M_{\text{tip}} = 0$$

Integrate Cosserat ODEs with RK4 along $s \in [0, L]$
Compute compliance $C(P) \in \mathbb{R}^{6\times 6}$ at the tip (from adjoint variables)
Predict incremental twist: $\delta\xi \leftarrow C(P)\,[F_d^\top \ 0^\top]^\top$
Extract translation: $\Delta p \leftarrow \begin{bmatrix} I_{3\times 3} & 0_{3\times 3} \end{bmatrix} \delta\xi$
Return Δp

4 Results

4.1 Simulation Results of Forward and Inverse Solvers

This section presents the simulation results of the developed forward and inverse kinematics solvers, together with their computational performance across MATLAB, C++, and MEX implementations. The simulations illustrate the predicted configurations of the soft robot under representative chamber pressure distributions and demonstrate the solver's ability to compute smooth trajectories and efficient actuation inputs.

4.1.1 Forward Kinematics Simulation

The forward kinematics solver predicts the spatial configuration of the soft robot by integrating the Cosserat rod equilibrium equations under applied chamber pressures. Figure 15 illustrates four representative configurations of the soft robot under different pressure distributions: In Figure 15(a), no pressure is applied $(p_1 = 0,\ p_2 = 0,\ p_3 = 0)$, the robot remains undeformed. In Figure 15(b), equal pressure $(p_1 = 1,\ p_2 = 1,\ p_3 = 1)$ is applied to all chamber pairs, resulting in a uniform elongation with minimal bending. In Figure 15(c), a higher pressure is applied to a single pair of chambers $(p_1 = 1.5,\ p_2 = 0,\ p_3 = 0)$, producing a unidirectional bend. Figure 15(d) shows a more complex shape by by combining different pressure levels $(p_1 = 1.5,\ p_2 = 1,\ p_3 = 0)$.

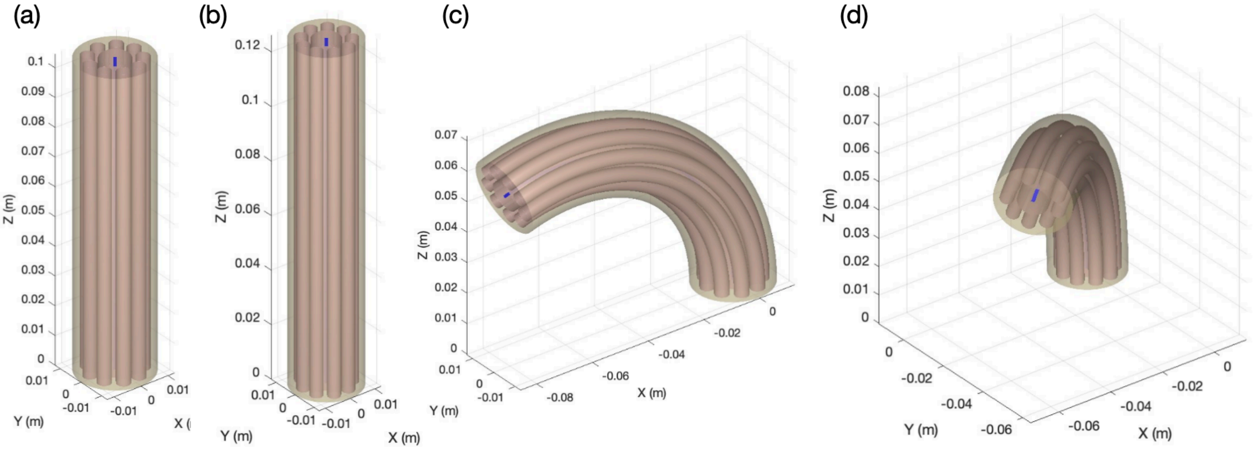

Figure 15: Final configurations of the soft robot under different pressure distributions: (a) $(p_1, p_2, p_3) = (0, 0, 0)$*, (b)* $(p_1, p_2, p_3) = (1, 1, 1)$*, (c)* $(p_1, p_2, p_3) = (1.5, 0, 0)$*, (d)* $(p_1, p_2, p_3) = (1.5, 1, 0)$

Table 3 compares the implementations of the forward solver across MATLAB, C++, and MEX-integrated platforms. While MATLAB provides flexibility for prototyping and visualisation, it requires approximately 30 ms per computation. In contrast, the optimised C++ implementation achieves a significant performance improvement, reducing the runtime to about 0.1 ms

Table 3: Comparison of forward kinematics implementations across MATLAB, C++, and MEX platforms

Aspect	**MATLAB**	**C++**	**MEX**
Numerical Integration	RK4	Custom RK4	MATLAB/C++ hybrid
Nonlinear Solver	`fsolve` (LM)	Custom LM solver	Interface to C++ solver
Visualization	Built-in plotting	External tools	MATLAB plotting
Execution Speed	30 ms	0.1 ms	0.3 ms
Ease of Implementation	High	Moderate	Moderate
Flexibility in Experimentation	High	Low	Medium

through Eigen-based numerical routines. The MEX interface integrates the C++ core within MATLAB, achieving near-native performance (0.3 ms) while preserving MATLAB's data acquisition and plotting capabilities, making it well-suited for integration into real-time control frameworks. All simulations were conducted on an HP Z2 Tower G9 Workstation equipped with an Intel Core i7-13700K CPU (24 threads, 3.4 GHz), 64 GB RAM, and an NVIDIA RTX A4000 GPU (16 GB VRAM), running Windows 11 Enterprise 64-bit.

4.1.2 Inverse Kinematics Simulation

The inverse kinematics solver computes the chamber pressures required to achieve a desired tip pose. Figure 16 presents the simulation results of the inverse kinematics solver for two representative circular trajectories. In case (a), the target trajectory has a radius of 0.06 m at a fixed height of 0.08 m, while in case (b), the radius is increased to 0.08 m at a lower height of 0.05 m. In both cases, the computed tip trajectories (red) closely follow the specified targets (blue), and the reconstructed centreline profiles (green) exhibit smooth and continuous deformations along the robot body, demonstrating the solver's capability to generate accurate actuation inputs.

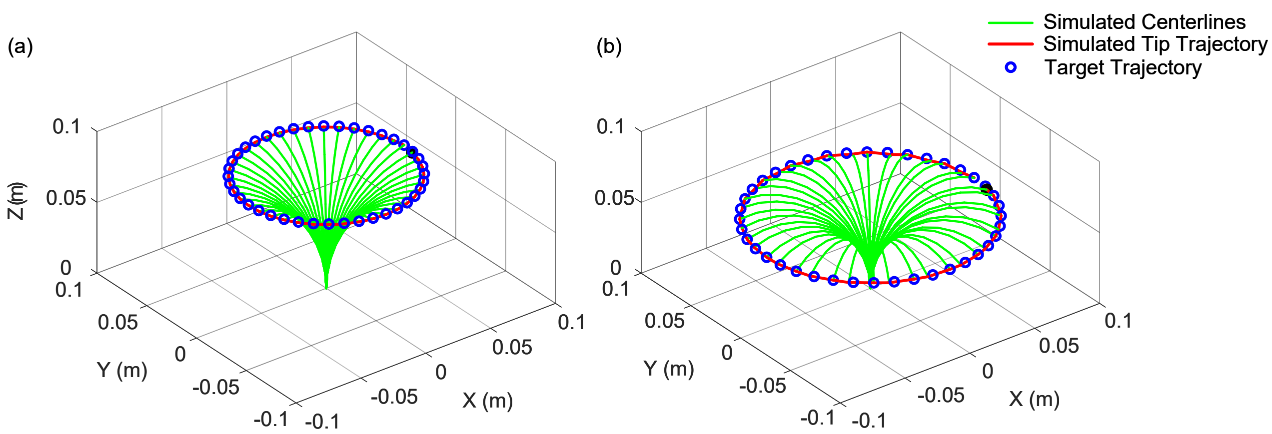

Figure 16: Simulation results of inverse kinematics tracking.

Table 4 summarises the computational performance of the inverse kinematics solver across MATLAB, C++, and MEX-integrated platforms. The MATLAB implementation requires approximately 40 ms per trajectory point, while the optimised C++ solver achieves a significant speedup, reducing the runtime to 0.2 ms. The MEX interface bridges MATLAB and C++, achieving near-native performance (0.4 ms) while retaining MATLAB's visualisation and data processing capabilities.

Table 4: Comparison of inverse kinematics implementations across MATLAB, C++, and MEX platforms

Aspect	**MATLAB**	**C++**	**MEX**
Numerical Integration	Reuse FK integrator	Reuse FK integrator	Reuse FK integrator
Nonlinear Solver	`fsolve` (LM)	Custom LM solver	Interface to C++ solver
Visualization	Overlay on FK plot	External tools	MATLAB plotting
Execution Speed	40 ms/point	0.2 ms	0.4 ms
Ease of Implementation	High	Moderate	Moderate
Flexibility in Experimentation	High	Low	Medium

These results demonstrate that the proposed inverse kinematics solver combines computational efficiency with accurate trajectory generation, providing a practical foundation for its subsequent use in experimental trajectory tracking and compliance regulation.

4.2 Parameter Identification in the Kinematics Model

4.2.1 Experimental Setup

To enable parameter identification and subsequent model refinement of the kinematics model, a dedicated experimental platform was constructed to impose stable and repeatable boundary conditions on the soft continuum robot. The setup was used for (i) bending tests under single- and double-chamber pressurisation to identify the pressure-dependent modulus $E(p)$, and (ii) trajectory-tracking trials to refine the fitted model.

The soft robot is vertically mounted using a rigid, 3D-printed support structure. The base of the robot is securely clamped at the centre of the fixture, enforcing zero translational and rotational motion at the proximal end. The support frame is bolted to an optical breadboard using standard M5 fasteners, providing a flat and low-vibration reference plane throughout all experiments. Tip pose is measured with the Aurora electromagnetic tracking system, and chamber pressures are commanded via the microcontroller Teensy 4.0.

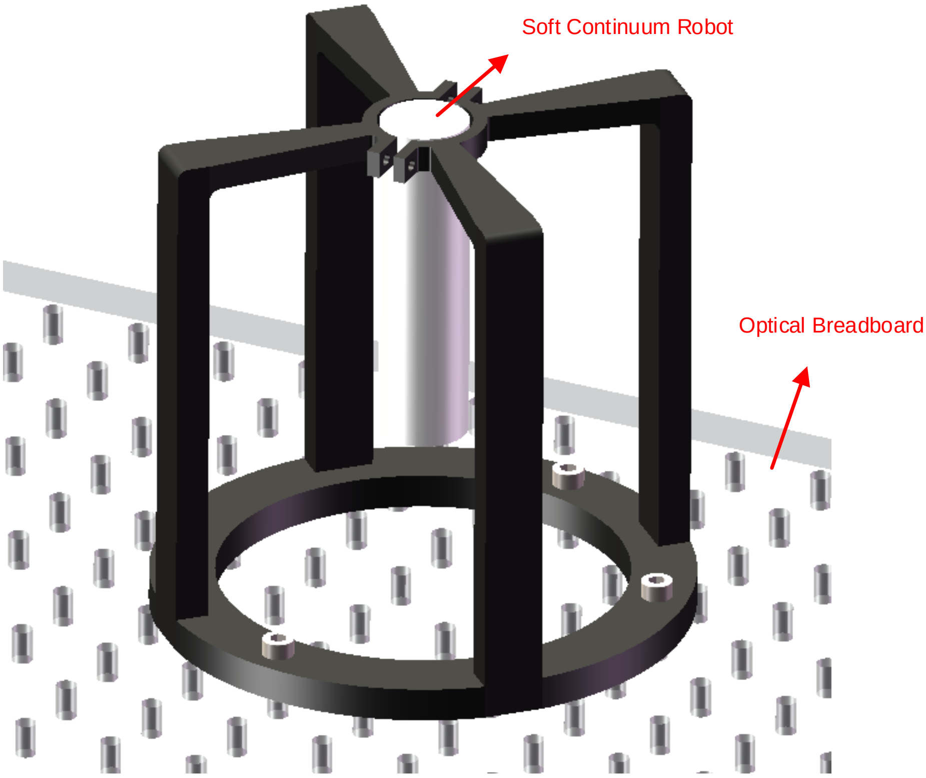

Figure 17: Experimental setup for parameter identification.

4.2.2 Identification of Material Modulus

Bending Angle Test. Tests of bending angles were conducted to identify the pressure-dependent effective modulus $E(p)$ of the soft actuator. Two actuation schemes were tested: (*i*) single-pair pressurisation, where one chamber pair was inflated while the other two remained unpressurised; and (*ii*) dual-pair pressurisation, where two chamber pairs were symmetrically inflated, generating bending toward the remaining unpressurised side. In both cases, the chamber pressure was quasi-statically increased from 0 to 2.0 bar in 0.1 bar increments. The corresponding bending angle θ_m in the bending plane was directly measured using the Aurora electromagnetic tracking system at each pressure step.

For each pressure level, the effective Young's modulus E was identified by minimising the difference between the model-predicted bending angle $\theta_{\text{model}}(E,p)$, computed from the Cosserat-rod forward solver, and the measured angle θ_m:

$$E^*(p) = \arg\min_E \left(\theta_{\text{model}}(E,p) - \theta_m\right)^2. \tag{23}$$

This procedure was repeated for all three single-pair and three dual-pair configurations, and the resulting $E_{\text{single}}(p)$ and $E_{\text{dual}}(p)$ curves were averaged to obtain the mean modulus curve $\bar{E}(p)$ for subsequent model fitting.

Inverse Kinematics Test. The pressure-dependent modulus $E(p)$ obtained from bending tests was fitted and incorporated into both the forward solver `FYP_BVP_Forward` and the inverse solver `FYP_Tip_Inverse`. To evaluate the predictive accuracy of the material modulus under multi-chamber actuation, a trajectory-tracking experiment was conducted. A reference circular trajectory $p_{\text{ref}}(t)$ with a radius of 30 mm and a constant height of 0.11 m was specified and uniformly sampled into 80 points. The corresponding chamber pressure profiles were computed using the inverse solver `FYP_Tip_Inverse` based on the fitted $E(p)$. These pressures were applied to the robot while the actual tip positions $p_m(t)$ were continuously recorded by the Aurora electromagnetic tracking system. The recorded trajectories were then compared with the reference trajectory to quantify the overall model accuracy. Figures 18(a)-(b) show the bending angle tests used to identify the pressure-dependent modulus $E(p)$. A hyperbolic tangent model was fitted to the averaged data using nonlinear least squares in MATLAB. According to Equation (23), the modulus under each pressure was computed and is reported in Figure 18(e). The resulting fitted curve is given by (units: E in kPa, p in bar):

$$E(p) = 246.83 + 44.13\,\text{tanh}\big(1.414 - 1.113\,p\big), \tag{24}$$

which provides a smooth approximation of the averaged bending data and serves as the baseline modulus model.

Figures 18(c)-(d) further evaluate the model accuracy under multi-chamber actuation using inverse kinematics control. Uniform offsets $\Delta E \in \{-15, -30, -45\}$ kPa were applied to the fitted curve, yielding $E^*(p) = E(p) + \Delta E$. Using the initial $E(p)$ led to an underestimation of bending, indicating that the modulus obtained from static bending slightly overestimated the effective stiffness under combined loading. Reducing E by a constant offset improved the agreement between model predictions and experimental results, with $\Delta E = -30$ kPa giving the best overall accuracy.

For the circular trajectory tracking experiment ($r = 30$ mm, $z = 0.11$ m, 80 points), the RMSE decreased from 5.52 mm with the original fit to 3.09 mm using $E^*(p)$, corresponding to a 44 % reduction. The mean bending angle errors under single- and dual-chamber actuation are $12.61°$ and $3.38°$, respectively, as shown in Figure 18(a). Accordingly, the optimised modulus model is expressed as:

$$E^*(p) = E(p) - 30 = 216.83 + 44.13\,\text{tanh}\big(1.414 - 1.113\,p\big). \tag{25}$$

This refined model is adopted in both the forward and inverse kinematic solvers for all subsequent trajectory tracking and compliance control experiments.

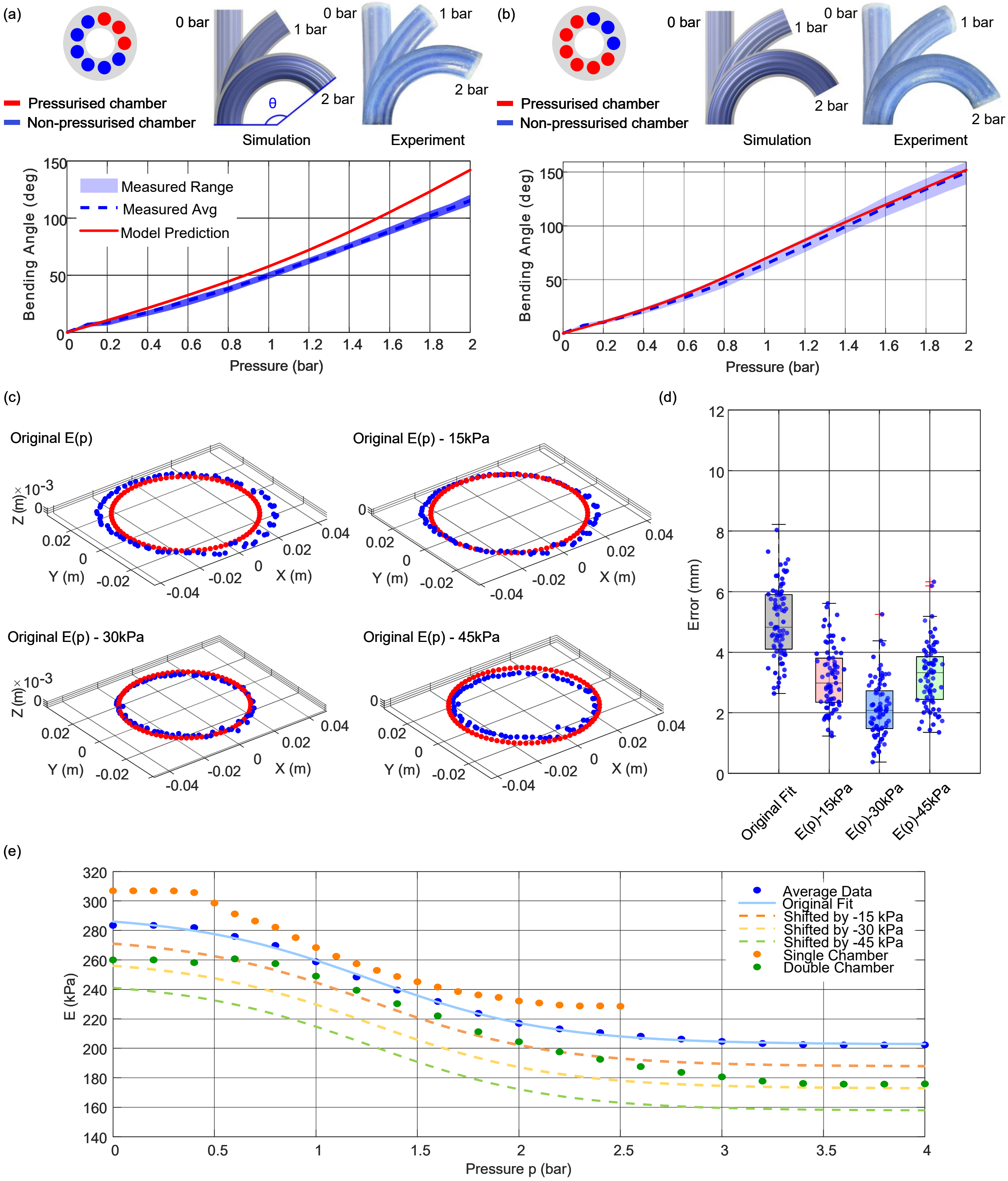

Figure 18: Experimental identification and refinement of the pressure-dependent modulus $E(p)$ and its validation on a circular trajectory tracking task. (a) Comparison of predicted and measured bending angles under single-chamber actuation. (b) Comparison of predicted and measured bending angles under dual-chamber actuation. (c) Circular trajectory tracking results ($r = 30\,$mm, $z = 0.11\,$m, 80 points) using the fitted model $E(p)$ and its shifted variants $E(p) + \Delta E$. (d) Tracking errors for different uniform offsets $\Delta E = \{0, -15, -30, -45\}\,$kPa. (e) Identified $E(p)$ curve from bending tests fitted using the hyperbolic tangent model.

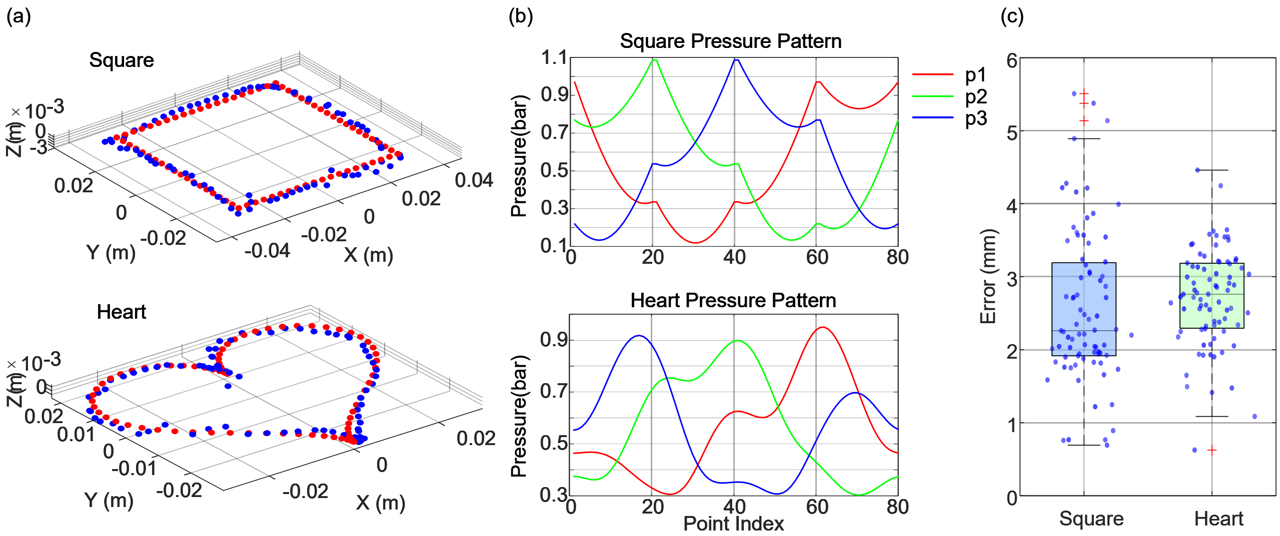

Figure 19: Cross validation of the fitted modulus model $E^*(p)$ using square and heart-shaped trajectories. (a) Measured vs. desired trajectories; (b) Chamber pressure profiles; (c) Tracking error distributions.

4.2.3 Cross Validation of Modulus in Different Trajectories

To further validate the efficacy of the identified material modulus curve in Equation (25), cross-validation experiments were conducted using two additional trajectories (a square path and a heart-shaped curve).

The square trajectory comprised four straight segments forming a closed square with a half-side length of 30 mm (60 mm full side), giving a total path length of 240 mm. The heart-shaped trajectory was generated parametrically, with a maximum width of 60 mm, height of 55 mm, and a total length of about 180 mm. Both trajectories were uniformly sampled into 80 points, with the z-coordinate fixed at 0.11 m.

At each step, the inverse kinematics solver `FYP_Tip_Inverse` calculated the chamber pressures p required to reach the desired tip positions p_d. These pressures were applied through the pressure regulator, and the resulting tip positions p_m were recorded in real time using the Aurora tracking system. The measured trajectories were then compared with the model-predicted trajectories p_{model} computed by the forward solver `FYP_BVP_Forward`. Figures 19(a) shows the tracking results for the square and heart-shaped trajectories using the refined modulus model $E^*(p)$. In both cases, the measured tip positions closely followed the desired paths, demonstrating accurate model prediction under multi-directional actuation. The corresponding chamber pressure profiles are shown in Figure 19(b), indicating smooth and coordinated actuation throughout the motion. Figure 19(c) summarises the tracking errors, where the RMSE was 3.02 mm for the square trajectory and 2.84 mm for the heart-shaped trajectory. These results confirm that the identified modulus $E^*(p)$ achieves reliable prediction accuracy and generalises well beyond the circular calibration trajectory.

4.3 Compliance Regulation Validation

4.3.1 Experimental Setup

Building upon the general support structure described in Section 4.2.1, an additional loading module was integrated to enable quantitative evaluation of the robot's directional compliance under external forces.

As shown in Figure 20, a custom loading fixture was mounted adjacent to the robot and aligned in the same horizontal plane. It consists of a two-axis translation frame with adjustable arms, allowing calibrated weights to be suspended from the robot tip along arbitrary planar directions. The fixture can be repositioned along the x and y axes, enabling repeatable and directional loading without disturbing the robot base.

To apply controlled forces, small calibrated weights (10 g to 50 g) are attached to a lightweight string passing through a low-friction pulley mounted on the loading arm, generating a consistent tip load along the selected direction. The robot tip position is recorded using the Aurora electromagnetic tracking system. By comparing the measured tip displacement under external loads, with and without active compliance regulation, the effectiveness of the proposed directional compliance control can be quantitatively evaluated.

4.3.2 Directional Compliance Validation

Directional stiffness was assessed by applying calibrated weights along the global x-, y-, and z-axes under different commanded stiffness gains (Figure 21). Two robot configurations were assessed. For each robot configuration and axis, stiffness was estimated independently from the load–displacement slope.

Vertical (z-) direction loading. To characterise stiffness along the z-axis, the chamber pressures were adjusted to achieve four target stiffness gain factors $k \in \{-20, 0, 20, 40\}$ N/m. Calibrated weights of 25 g and 50 g were suspended vertically from the distal tip to generate known external forces, as illustrated in Figure 21(a). For each commanded stiffness setting and load level, the resulting vertical tip displacement Δd_z was recorded in real time using the Aurora electromagnetic tracking system, and the directional stiffness and compliance were calculated as:

$$K_z = \frac{F}{\Delta d_z} \tag{26}$$

$$C_z = \frac{1}{K_z}, \tag{27}$$

Figure 20: Experimental setup for compliance regulation validation

where F is the applied vertical force.
For z-direction tests, the two robot configurations were defined as:

- **Configuration 1:** $p_1 = 0.8\,\text{bar},\ p_2 = p_3 = 0 \quad$ (bending along the $-x$ axis).
- **Configuration 2:** $p_1 = 1.0\,\text{bar},\ p_2 = p_3 = 0 \quad$ (bending along the $-x$ axis).

Lateral (x-, y-) direction loading. Similarly, the stiffness along the x- and y-axes was characterised by setting the commanded stiffness coefficient to $k \in \{-5, 0, 5, 10\}$ N/m and applying calibrated weights of $10\,\text{g}$, $20\,\text{g}$, and $30\,\text{g}$ along the positive global x- or y-axis, as illustrated in Figure 21(b). In each case, the applied load generated a known force F, and the corresponding tip displacements Δd_x and Δd_y were measured using the same tracking system to compute directional stiffness or compliance as:

$$K_x = \frac{F}{\Delta d_x}, \qquad K_y = \frac{F}{\Delta d_y}, \tag{28}$$

$$C_x = \frac{1}{K_x}, \qquad C_y = \frac{1}{K_y}. \tag{29}$$

For x/y-direction tests, the two robot configurations were chosen as:

- **Configuration 1:** $p_1 = 0.5\,\text{bar},\ p_2 = p_3 = 0 \quad$ (bending along the $-x$ axis).

- **Configuration 2:** $p_2 = 0.5\,\text{bar}$, $p_1 = p_3 = 0$ (bending towards both the $-y$ and $+x$ axes).

All measurements were performed for both configurations and repeated three times for each combination of stiffness setting and applied load. The average displacement across trials was used to calculate the reported stiffness values.

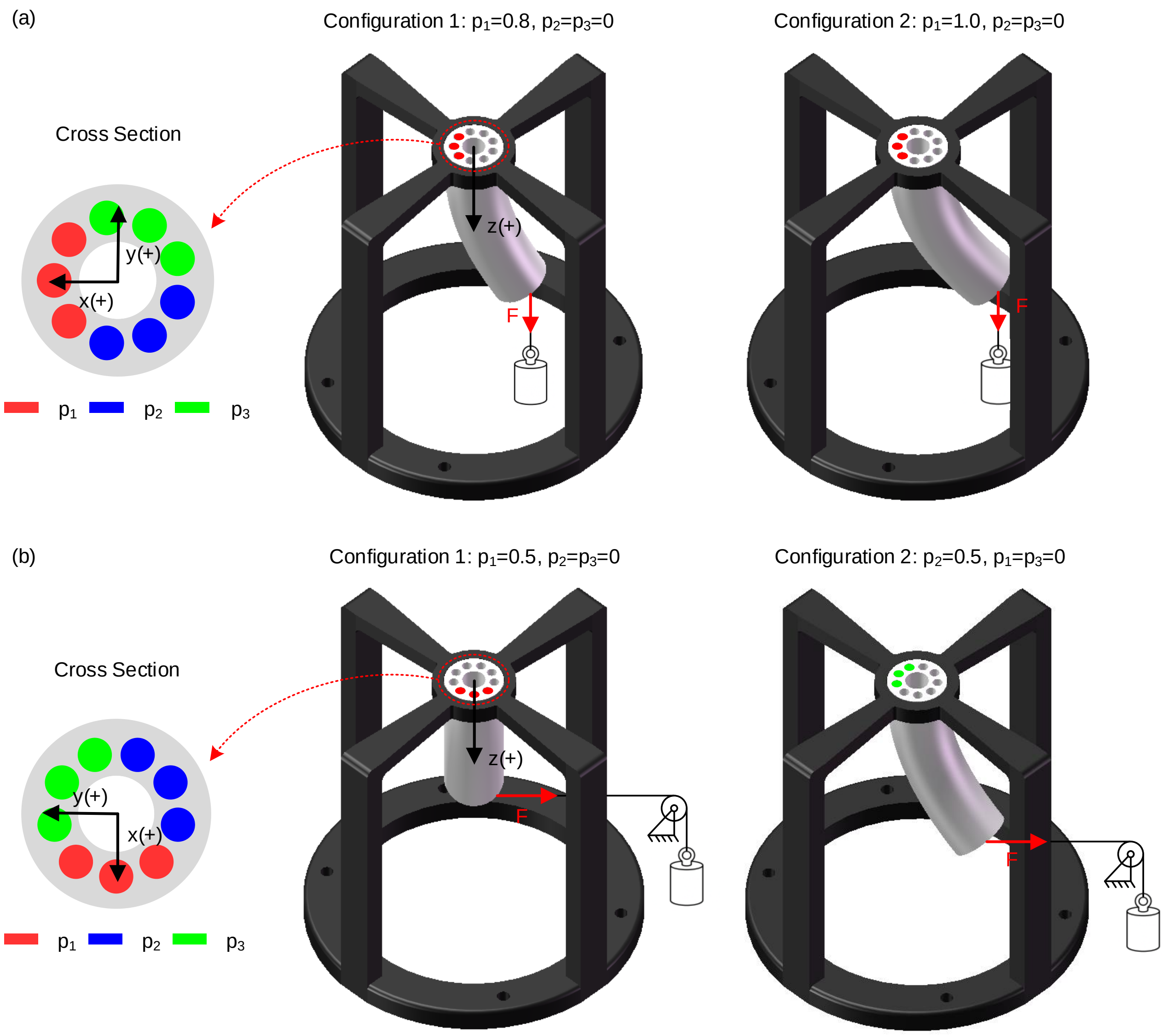

Figure 21: Experimental setup for directional loading tests. (a) z-direction loading under two configurations ($p_1 = 0.8\,\text{bar}$ and $p_1 = 1.0\,\text{bar}$). (b) x- and y- direction loading under two configurations ($p_1 = 0.5\,\text{bar}$ and $p_2 = 0.5\,\text{bar}$).

Results of vertical (z-) direction loading. Figures 22(a) - (b) show the deflection–load relationships for Configurations 1 and 2, respectively. For Configuration 1, the baseline compliance at $k_z = 0$ was $0.10\,\text{mm}\,\text{g}^{-1}$. When the gain was decreased to $k_z = -5$, the compliance increased to $0.13\,\text{mm}\,\text{g}^{-1}$, representing a $30\,\%$ variation relative to the baseline, and it corresponds to a noticeable softening effect. Conversely, increasing the gain to $k_z = 10$ reduced the compliance to $0.06\,\text{mm}\,\text{g}^{-1}$, corresponding to a $-40\,\%$ variation relative to the baseline, demonstrating a clear stiffening response. For Configuration 2, the compliance was generally higher due to the larger bending angle, with a baseline value of $0.16\,\mathrm{mm\,g^{-1}}$ at $k_z = 0$. At $k_z = -5$, the compliance further increased to $0.25\,\mathrm{mm\,g^{-1}}$, representing a $20.83\,\%$ variation relative to the baseline and thus exhibiting a softening effect. In contrast, increasing the gain to $k_z = 10$ significantly reduced the compliance to $0.08\,\mathrm{mm\,g^{-1}}$, corresponding to a $-50\,\%$ variation relative to the baseline, resulting in a pronounced stiffening effect.

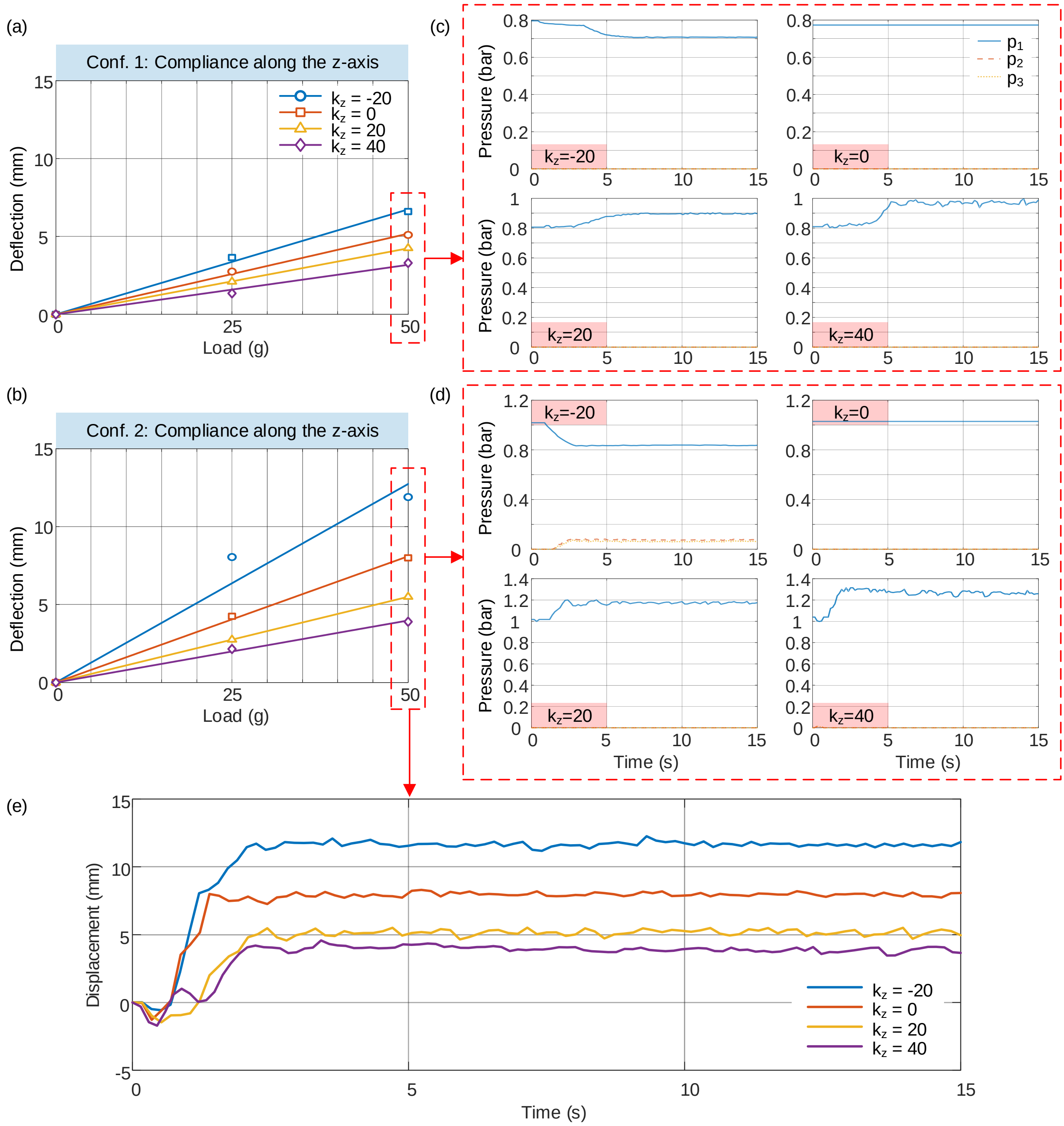

Figure 22: Experimental results of directional stiffness validation under z- direction loading. (a) Deflection–load relationships for Configuration 1. (b) Deflection–load relationships for Configuration 2. (c) Pressure responses of p_1, p_2, and p_3 in Configuration 1 under a $50\,\mathrm{g}$ vertical load for four k_z settings ($k_z = -20, 0, 20, 40$). (d) Pressure responses of p_1, p_2, and p_3 in Configuration 2 under a $50\,\mathrm{g}$ vertical load for four k_z settings ($k_z = -20, 0, 20, 40$). (e) Time responses of end-tip displacement in Configuration 2 under a $50\,\mathrm{g}$ vertical load for four k_z settings.

Table 5: Compliance along the z-axis under different gain factors (Colors highlight variation ratios: positive=red, zero=gray, negative=blue.)

		Configuration 1		Configuration 2	
	Gain factor	**Compliance [mm/g]**	**Variation ratio**	**Compliance [mm/g]**	**Variation ratio**
Compliance along the z-axis	$k_z = -20$	0.13	30.00%	0.25	20.83%
	$k_z = 0$	0.10	0%	0.16	0%
	$k_z = 20$	0.08	-20.00%	0.11	-31.25%
	$k_z = 40$	0.06	-40.00%	0.08	-50.00%

Figures 22(c) - (d) present the corresponding chamber pressure responses under a constant 50 g vertical load for the four k_z settings. As observed from the figures, for both Configuration 1 and 2, only p_1 was actively modulated to regulate vertical stiffness, while p_2 and p_3 remained zero throughout the experiments. For the baseline case ($k_z = 0$), the steady-state pressure of p_1 was approximately 0.5 bar. Increasing k_z above zero required raising p_1 above the baseline to stiffen the structure, whereas negative gain settings reduced p_1 below 0.5 bar, resulting in higher compliance.

Figure 22(e) further shows the transient tip displacement responses in Configuration 2, where the deflection rapidly stabilises within approximately 5 s, demonstrating consistent steady-state compliance under different stiffness settings.

Table 5 summarizes the measured compliance and variation ratios relative to the baseline for both configurations. Positive variation ratios indicate an increase in compliance (softening), while negative ratios indicate a decrease (stiffening).

Overall, these results confirm that the commanded stiffness gain k_z effectively modulates the vertical compliance of the robot, and the modulation effect becomes more pronounced with larger absolute gain values, as the change at $k_z = 40$ is significantly greater than that at $k_z = 20$. Additionally, Configuration 2 consistently exhibits higher compliance than Configuration 1 across all stiffness settings, indicating that larger bending angles reduce the effective vertical stiffness of the soft continuum robot.

Results of lateral (x-, y-) direction loading. Figure 23(a) show the deflection–load curves along the x- axis for Configuration 1. The baseline compliance along x- direction at $k_x = 0$ was 0.62 mm g^{-1}. Reducing the gain to $k_x = -5$ increased compliance to 1.59 mm g^{-1} (156.45 %, softening), while increasing the gain to $k_x = 10$ decreased it to 0.33 mm g^{-1} (-46.77 %, stiffening). Figure 23(c) show the corresponding chamber pressure responses. At the baseline $k_x = 0$, $p_1 \approx 0.5$ bar while $p_2 = p_3 \approx 0$ bar. When $k_x = -5$, p_1 decreases significantly, whereas p_2 and p_3 increase symmetrically, producing the observed softening. For $k_x = 5$

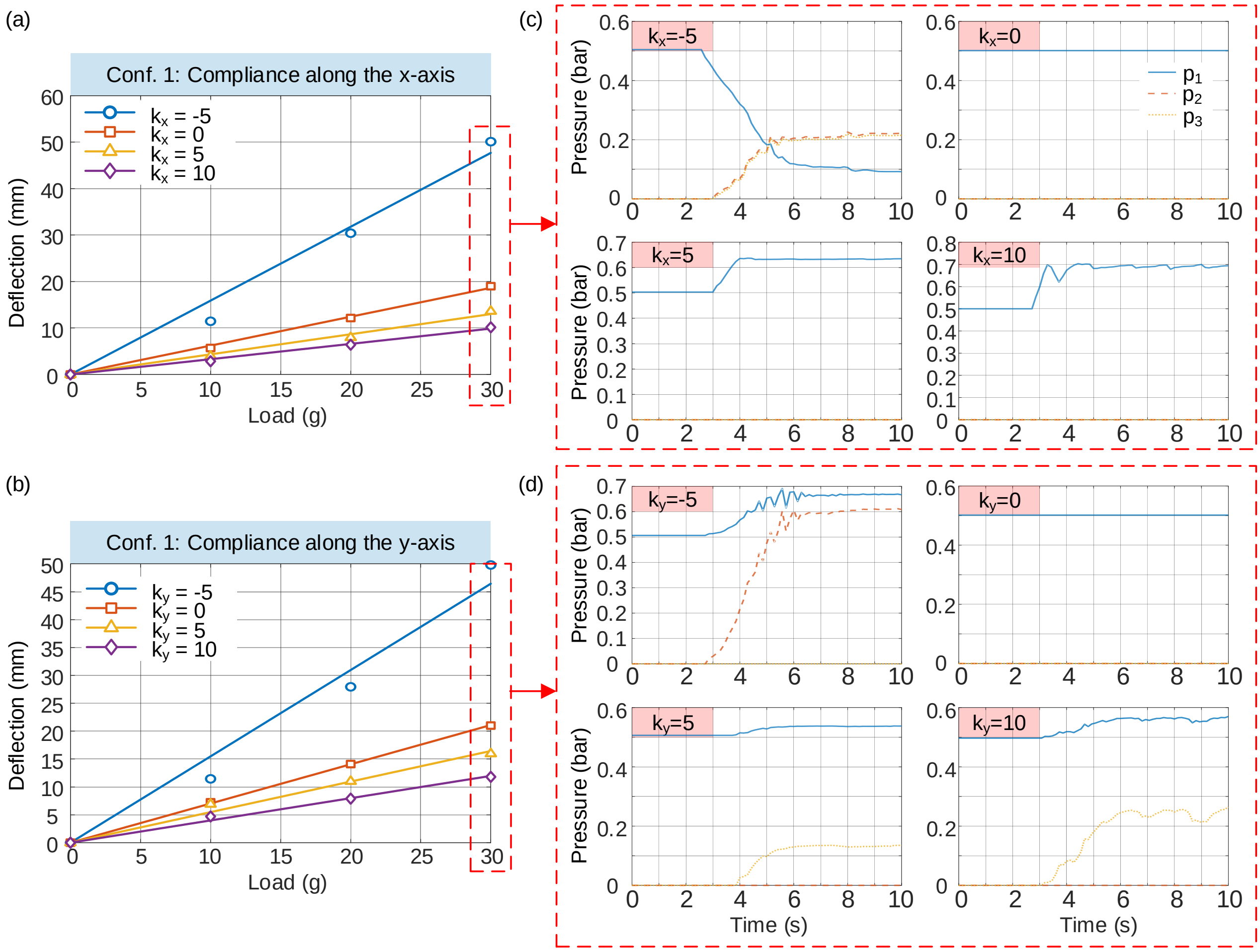

Figure 23: Experimental results of directional stiffness validation under x- and y- direction loading. (a) Deflection–load relationships along the x-axis. (b) Deflection–load relationships along the x-axis. (c) Pressure responses of p_1, p_2, and p_3 under a $30\,\mathrm{g}$ lateral load for four k_x settings ($k_x = -5, 0, 5, 10$). (d) Pressure responses of p_1, p_2, and p_3 under a $30\,\mathrm{g}$ lateral load for four k_y settings ($k_y = -5, 0, 5, 10$).

and $k_x = 10$, p_1 increases above baseline to enhance stiffness, while p_2 and p_3 remain close to zero.

Figure 23(b) show the deflection–load curves along y- axis for Configuration 1.The baseline compliance along y- direction at $k_y = 0$ was $0.70\,\mathrm{mm\,g^{-1}}$. At $k_y = -5$, the compliance increased to $1.55\,\mathrm{mm\,g^{-1}}$ ($121.43\,\%$, softening), while $k_y = 10$ reduced it to $0.40\,\mathrm{mm\,g^{-1}}$ ($-42.86\,\%$, stiffening). Figure 23(d) show the chamber pressures during y-axis regulation. At $k_y = 0$, $p_2 \approx 0.5$ bar and $p_1 = p_3 \approx 0$ bar. For $k_y = -5$, p_1 and p_2 both increase, the structure softens. For $k_y = 5$ and $k_y = 10$, p_1 increases slightly, p_3 increases notably, while p_2 remain near zero, leading to structural stiffening.

Figure 24(a) show the deflection–load curves along the x- axis for Configuration 2. The baseline compliance along x- direction at $k_x = 0$ was $0.67\,\mathrm{mm\,g^{-1}}$. At $k_x = -5$, compliance increased to $1.29\,\mathrm{mm\,g^{-1}}$ ($92.53\,\%$, softening), whereas $k_x = 10$ reduced it to $0.39\,\mathrm{mm\,g^{-1}}$ ($-41.79\,\%$, stiffening). Figure 24(c) show the pressure responses during x-axis regulation.

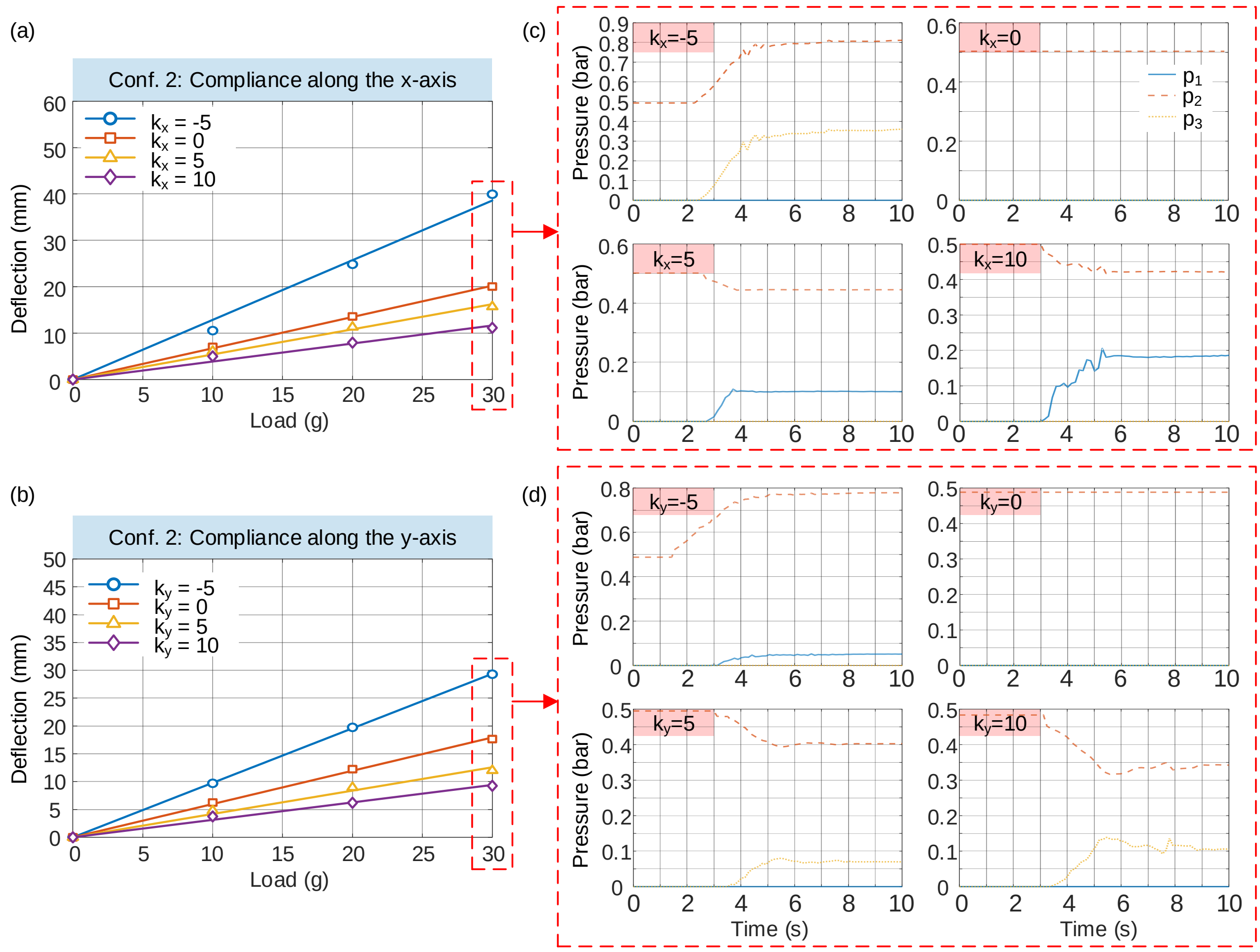

Figure 24: Experimental results of directional stiffness validation under x- and y- direction loading (Configuration 2). (a) Deflection–load relationships along the x-axis. (b) Deflection–load relationships along the x-axis. (c) Pressure responses of p_1, p_2, and p_3 under a 30 g lateral load for four k_x settings ($k_x = -5, 0, 5, 10$). (d) Pressure responses of p_1, p_2, and p_3 under a 30 g lateral load for four k_y settings ($k_y = -5, 0, 5, 10$).

At $k_x = 0$, $p_2 \approx 0.5$ bar and $p_1 = p_3 \approx 0$ bar. For $k_x = -5$, p_2 and p_3 both increase while p_1 remains near zero, resulting in softening. For $k_x = 5$ and $k_x = 10$, p_2 decreases below baseline while p_1 increases, redistributing forces to stiffen the structure.

Figure 24 (b) show the deflection–load curves along the y- axis for Configuration 2. The baseline compliance along y- direction at $k_y = 0$ was 0.60 mm g^{-1}. At $k_y = -5$, compliance increased to 0.98 mm g^{-1} (63.33 %, softening), while $k_y = 10$ reduced it to 0.31 mm g^{-1} (-48.33 %, stiffening). Figures 24 (d) show the chamber pressures during y-axis regulation. At $k_y = 0$, $p_2 \approx 0.5$ bar and $p_1 = p_3 \approx 0$ bar. For $k_y = -5$, p_2 increases significantly while $p_1, p_3 \approx 0$, enhancing softening. For $k_y = 5$ and $k_y = 10$, p_2 decreases below baseline and p_1 increases, shifting force contribution to achieve stiffening.

Table 6 summarises the measured lateral compliance and variation ratios for both configurations. Across all cases, negative gains ($k_{x/y} < 0$) lead to increased compliance (softening),

Table 6: Compliance along the x- and y-axes under different gain factors.

		Configuration 1		Configuration 2	
	Gain factor	**Compliance [mm/g]**	**Variation ratio**	**Compliance [mm/g]**	**Variation ratio**
Compliance along the x-axis	$k_x = -5$	1.59	156.45%	1.29	92.53%
	$k_x = 0$	0.62	0%	0.67	0%
	$k_x = 5$	0.43	-30.65%	0.54	-19.40%
	$k_x = 10$	0.33	-46.77%	0.39	-41.79%
Compliance along the y-axis	$k_y = -5$	1.55	121.43%	0.98	63.33%
	$k_y = 0$	0.70	0%	0.60	0%
	$k_y = 5$	0.55	-21.43%	0.42	-30.00%
	$k_y = 10$	0.40	-42.86%	0.31	-48.33%

while positive gains ($k_{x/y} > 0$) reduce compliance (stiffening), and the tuning effect becomes more significant at larger gain values (e.g., $k = 10$ shows much stronger stiffening than $k = 5$). Compared with the vertical direction, the lateral directions exhibit a higher baseline compliance, and a smaller commanded gain factor is sufficient to achieve a comparable modulation range.

This section validates the efficacy and range of the compliance regulation at specific static robot configurations. Simultaneous position-compliance control can also be achieved and will be demonstrated in the following sections.

4.4 Application of Compliance Regulation

Three experiments are conducted to demonstrate applications of the compliance regulation, including i) active interaction control, ii) position and compliance-stiffening control for trajectory holding and iii) position and compliance-softening control for obstacle avoidance.

4.4.1 Active Interaction Control

In this experiment, the robot was first actuated to a fixed reference pose ($p_1 = 0.5$ bar, $p_2 = p_3 = 0$). Three trials were performed with directional stiffness commands $K =$ diag$(10, 0, 0)$, diag$(0, 10, 0)$, and diag$(0, 0, 10)$, respectively. During each trial, fingertip applies forces to the robot's tip in three stages: stage 1-along $+x$ and $-x$ axes; stage 2-along $+y$ and $-y$ axes; stage 3-along $+z$ and $-z$ axes, as demonstrated in Figure 25. Chamber pressures (p_1, p_2, p_3) and Cartesian tip positions (x, y, z) were recorded during the tests (total duration ≈ 25 s). Figure 26 shows the results under three virtual stiffnesses: $K =$ diag$(10, 0, 0)$, $K =$ diag$(0, 10, 0)$, and $K =$ diag$(0, 0, 10)$.

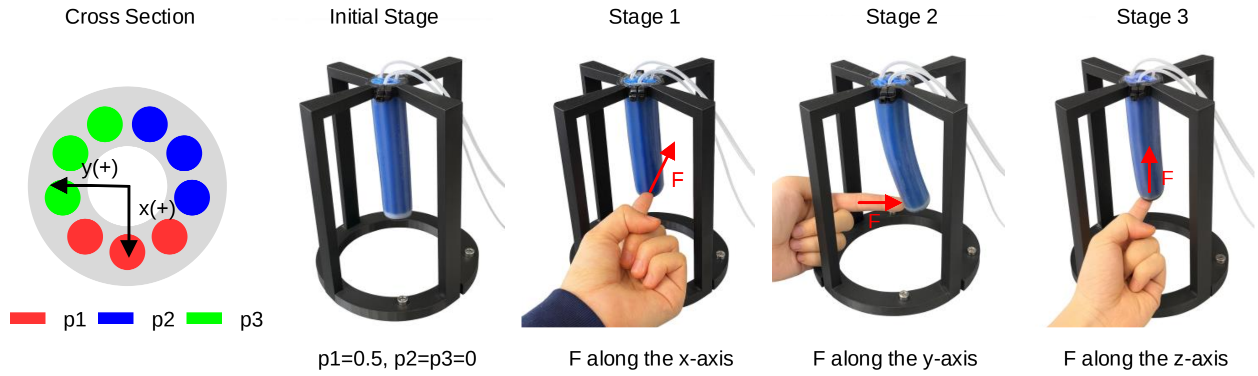

Figure 25: Experimental setup for manual disturbance tests. The robot was held at a fixed reference pose ($p_1 = 0.5$ bar, $p_2 = p_3 = 0$), and fingertip perturbations were applied along the x-, y-, and z-axes (stage 1–3). Red, blue, and green indicate chambers p_1, p_2, and p_3.

As shown in Figure 26(a), the chamber pressures (p_1, p_2, p_3) exhibit distinct variations during the interaction periods. For $K = \text{diag}(10, 0, 0)$, when the interaction is applied along $+x$ axis, p_1 increases significantly while p_2 and p_3 remain nearly zero; when the interaction is applied along $-x$ axis, p_1 decreases while p_2 and p_3 increase simultaneously. When the forces are applied along the y-axis, p_1 exhibits small fluctuations while p_2 and p_3 remain zero. When the interaction is applied along the $-z$, p_1 decreases while p_2 and p_3 increase simultaneously; when the interaction is applied along $+z$ axis, p_1 increases significantly while p_2 and p_3 remain zero. For $K = \text{diag}(0, 10, 0)$, when the interaction is applied along $-y$ axis, p_3 increases markedly, p_1 also increases, while p_2 remains nearly constant; when the interaction is applied along $+y$ axis, p_2 increases significantly, p_1 shows a slight increase, while p_3 remains close to zero. When the forces are applied along the x and z axes, p_1, p_2, and p_3 remain approximately constant. For $K = \text{diag}(0, 0, 10)$, when the interaction is applied along $-z$ axis, p_1 decreases while p_2 and p_3 remain nearly constant; when the interaction is applied along $+z$, p_1 shows a small increase while p_2 and p_3 remain stable. When perturbations are applied along the x and y axes, p_1, p_2, and p_3 are close to invariant.

Figure 26(b) presents the corresponding tip positions (x, y, z) during the experiments. Specifically, during stage 1 when perturbations are applied along $-x$ axis, the tip position x decreases, and when the perturbations are reversed along the $+x$ axis, x increases correspondingly, while y and z remain nearly constant. During stage 2 with perturbations along the y axis, y exhibits negative and positive shifts while x and z stay close to baseline, and in stage 3, z decreases under perturbations along the $-z$ axis and increases under perturbations along the $-z$ axis, x also exhibits negative and positive and, while y remains stable.

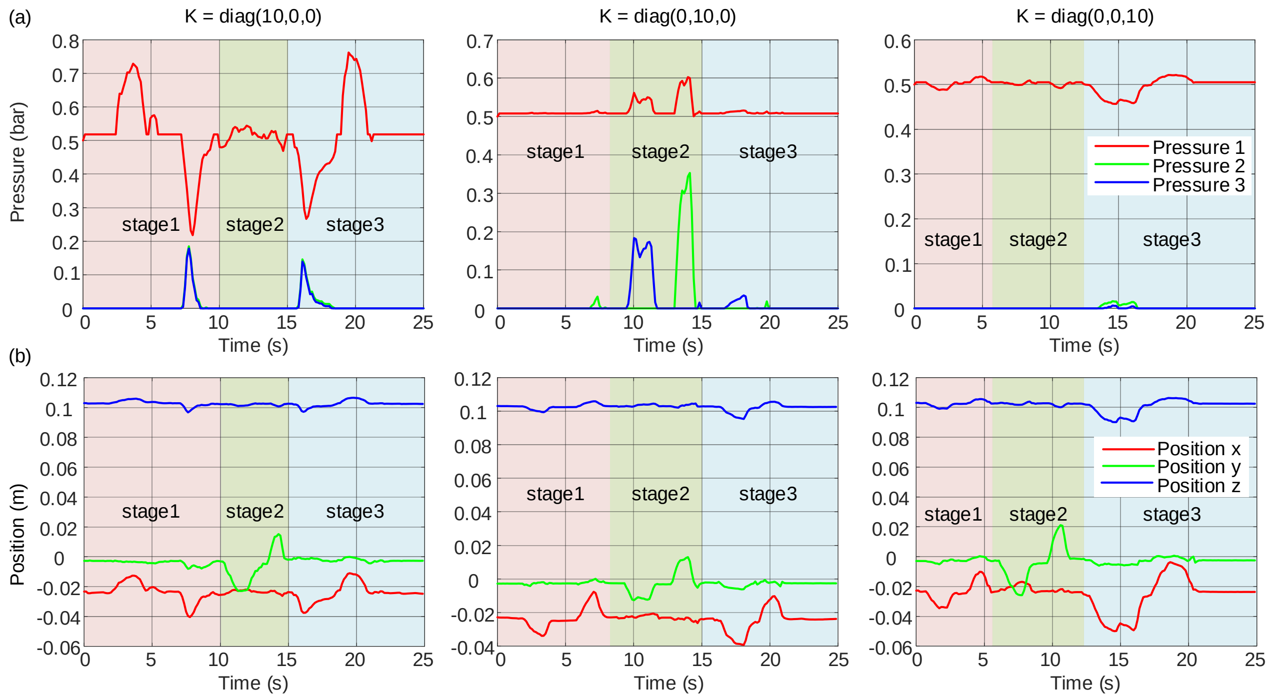

Figure 26: Experimental results of manual disturbance tests under different directional stiffness configurations. (a) Pressure responses of the three chambers when fingertip perturbations were applied sequentially along the x-, y-, and z-axes (stage 1–3). (b) Corresponding changes in tip position along the x, y, and z axes.

4.4.2 Position and Compliance-Stiffening Control for Trajectory Holding

The robot was commanded to follow prescribed trajectories with different stiffening factors under external loads, as shown in Figure 27. Three experiments were tested based on two trajectories: (i) **Straight trajectory with in-line loading** (Figure 27(e)): A line of half-length $L = 0.035$ m was tracked along the x-axis. External loads of 10 g and 20 g were applied along the $+x$ axis via a low-friction pulley, while varying $k_x \in \{0, 1.25, 2.5, 3.75, 5\}$ and keeping $k_y = k_z = 0$; (ii) **Circular trajectory with in-plane loading** (Figure 27(b,f)): A circle of a radius $R = 0.025$ m was commanded in the x–y plane. In-plane disturbances (10 g or 20 g) were applied via a pulley system (Figure 27(b)), with the force direction varies with the robot pose. Stiffness parameters were set as $k_x = k_y \in \{0, 1.25, 2.5, 3.75, 5\}$; (iii) **Circular trajectory with vertical loading** (Figure 27(c,f)): The same circular path was tracked under a constant 20 g vertical load along $+z$ axis (Figure 27(c)), while varying $k_z \in \{0, 10, 20\}$ and keeping $k_x = k_y = 0$. For all conditions, the robot was first positioned at the trajectory start point. After attaching the load, the commanded trajectory was followed while continuously recording the tip position and chamber pressures. Each configuration was tested for all stiffness and load combinations, and every trial was repeated three times for repeatability.

Results of straight trajectory holding with in-line loading. Figure 28 shows the measured trajectories under a 20 g external loading for different commanded stiffness gains k_x. In the

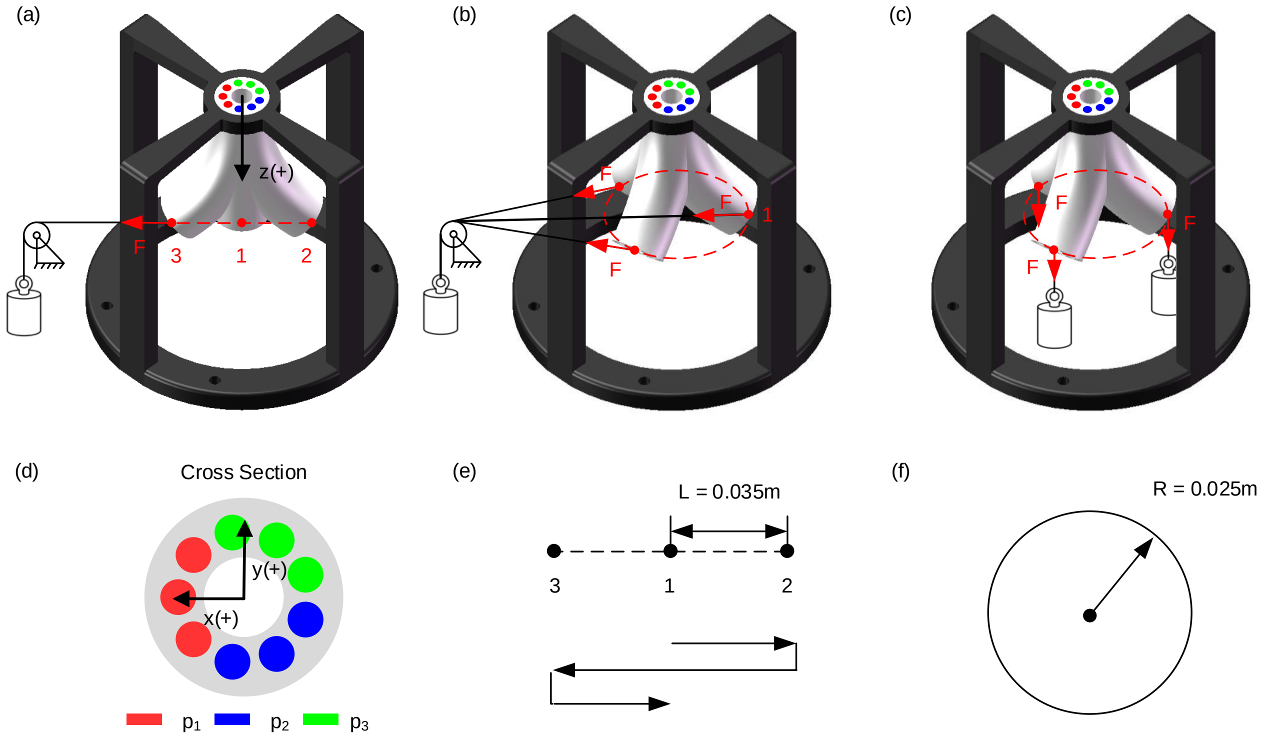

Figure 27: Experimental setup for trajectory holding under external loads. (a) Straight trajectory with in-line loading F ($10\,$g or $20\,$g) along $+x$. (b) Circular trajectory with in-plane loading F ($10\,$g or $20\,$g) following the path direction. (c) Circular trajectory with vertical loading F ($20\,$g) along $+z$. (d) Cross-section showing pneumatic chambers (p_1, p_2, p_3) and coordinate axes. (e) Straight trajectory with half-length $L = 0.035\,$m. (f) Circular trajectory with radius $R = 0.025\,$m.

baseline case without external loading ($k_x = 0$, $load = 0\,$g), the end-tip accurately followed the desired path with negligible deviation. When a $20\,$g load was applied along the $+x$ axis without stiffness regulation ($k_x = 0$), the end-tip exhibited a noticeable drift along the loading direction. By increasing k_x, the measured trajectories became progressively closer to the desired straight line.

Figure 29 summarises the distribution of tejectory control errors subject to different loads and stiffness gain parameters. For the $10\,$g load, the RMSE decreased from $10.8\,$mm at $k_x = 0$ to $5.9\,$mm at $k_x = 5$, corresponding to a $45\,$% reduction. Under the $20\,$g load, the RMSE decreased from $20.7\,$mm at $k_x = 0$ to $13.0\,$mm at $k_x = 5$, representing a $37\,$% reduction.

To evaluate the statistical significance of these improvements, pairwise Welch's t-tests were performed for all stiffness gains under each loading condition. For the $10\,$g load, most pairwise comparisons yielded highly significant differences ($p < 0.001$), indicating that increasing k_x effectively reduced the trajectory error. Similarly, for the $20\,$g load, the difference between $k_x = 0$ and $k_x = 5$ was highly significant ($p < 0.001$), while the reduction from $k_x = 3.75$ to $k_x = 5$ was not statistically significant ($p = 0.85$). These results confirm that higher stiffness gains enhance the robot's ability to maintain the desired trajectory when subjected to external

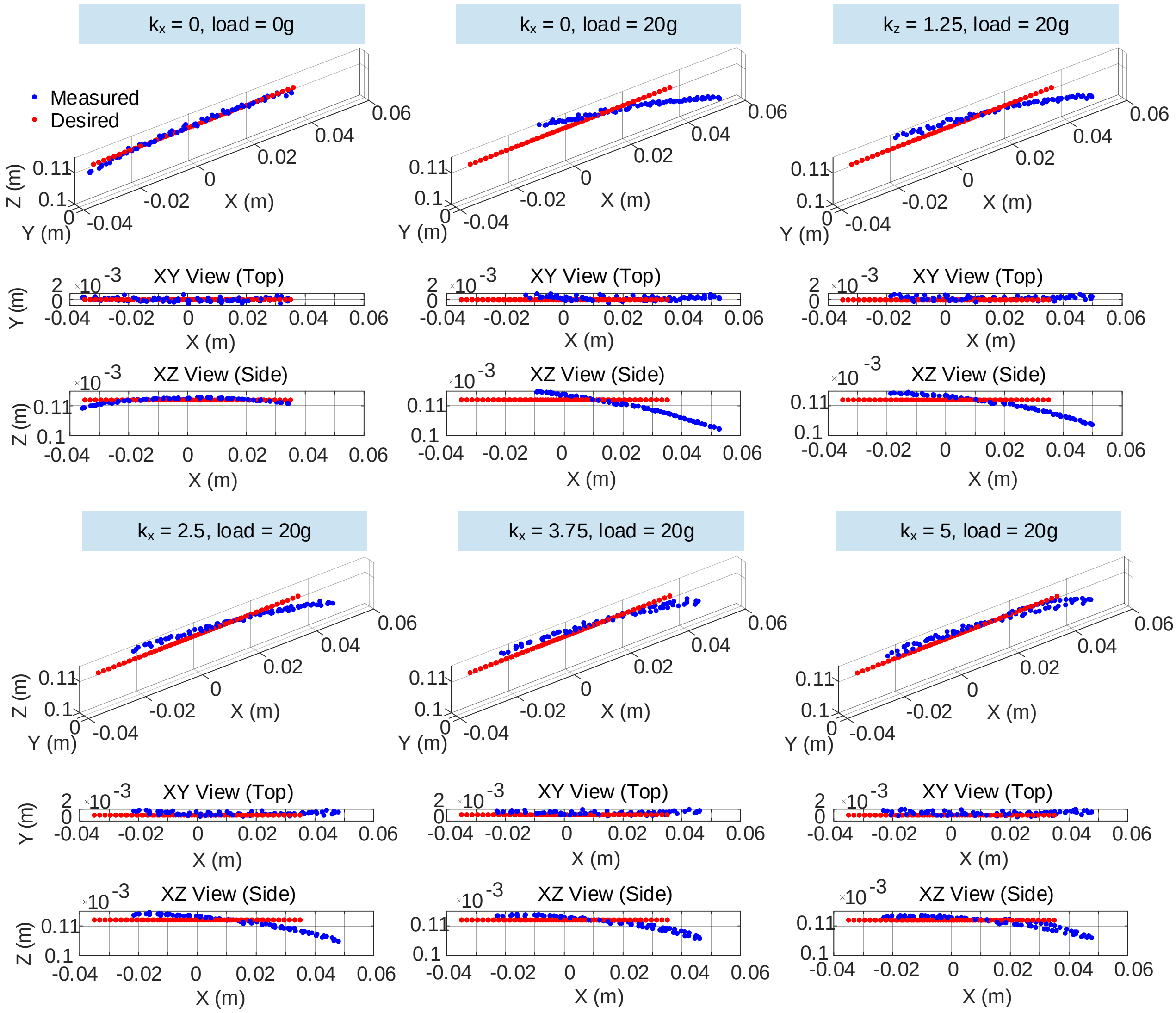

Figure 28: Straight-line trajectory holding performance under different stiffness gains $k_x = 0,\ 1.25,\ 2.5,\ 3.75,\ 5$ *with a* $20\,\mathrm{g}$ *external load, shown in 3D, top, and side views.*

loads, although the improvement becomes marginal at larger k_x values.

Figure 30 compares the chamber pressure profiles (p_1, p_2, p_3) during straight-line trajectory holding under a $20\,\mathrm{g}$ external load for $k_x = 0$ and $k_x = 5$. Without regulation, the pressures are dynamically modulated to track the trajectory. With $k_x = 5$, p_1 shifts upward while p_2 and p_3 shift downward. At the first endpoint (index ≈ 20), p_1 increases from 1.04 bar to 1.09 bar, while p_2 and p_3 decrease from 0.57 bar and 0.54 bar to 0.48 bar and 0.45 bar, respectively. At the second endpoint (index ≈ 60), p_1 rises from 0.41 bar to 0.51 bar, whereas p_2 and p_3 reduce slightly from 0.98 bar and 0.94 bar to 0.96 bar and 0.92 bar. Overall, stiffness regulation introduces an additional offset of up to $\Delta p \approx 0.10$ bar for p_1 and about 0.09 bar reduction for p_2 and p_3.

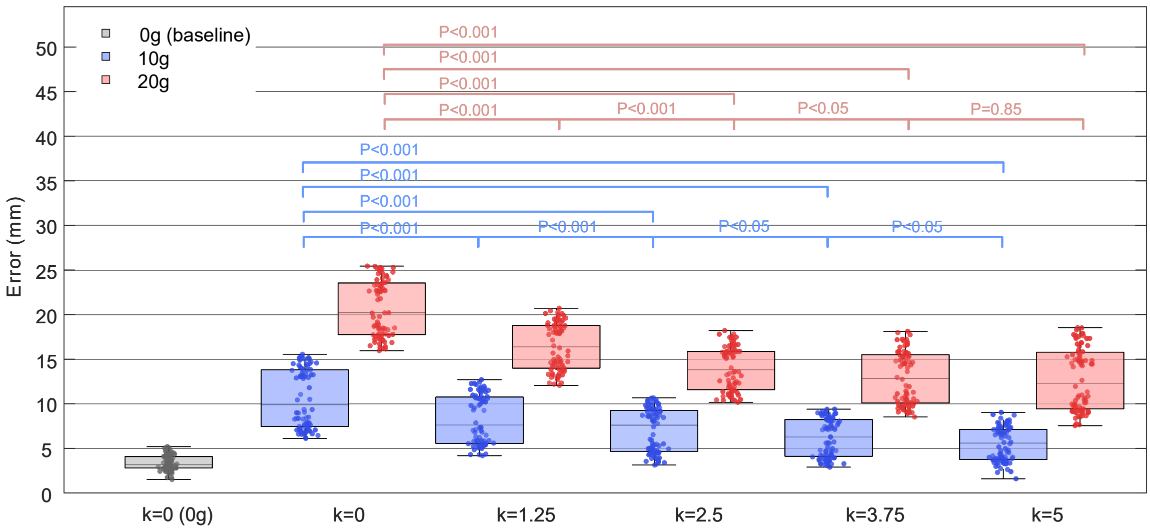

Figure 29: Tracking error for straight-line trajectory holding under different stiffness gains $k_x = 0,\ 1.25,\ 2.5,\ 3.75,\ 5$ with external loads of 0 g (baseline), 10 g, and 20 g.

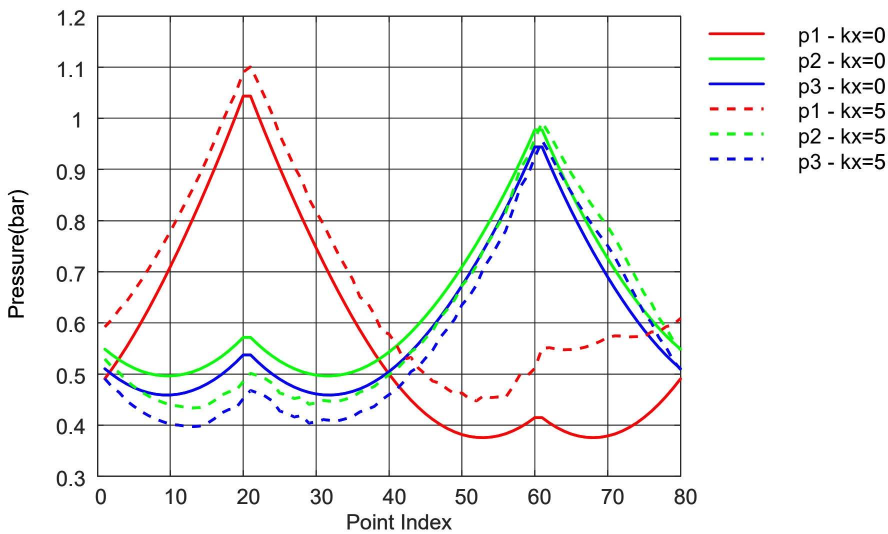

Figure 30: Chamber pressure profiles (p_1, p_2, p_3) during straight-line trajectory holding under different stiffness gains with a 20 g external load.

Results of circular trajectory holding with in-plane loading. Figure 31 shows the measured circular trajectories for different stiffness gain factors ($k_x = k_y \in \{0, 1.25, 2.5, 3.75, 5\}$) under a 20 g in–plane loads. Compared with the unloaded baseline, applying an in-plane disturbance caused clear deviations from the desired path. The deviations decreased as the commanded stiffness gain factors increased.

Figure 32 summarises the tracking errors. Under the 10 g load, the RMSE decreased from 11.93 mm at $k = 0$ to 6.69 mm at $k = 5$, corresponding to a 44 % reduction. Similarly, under the 20 g load, the 3D RMSE decreased from 22.27 mm at $k = 0$ to a minimum of 14.33 mm at $k = 3.75$ (36 % reduction), before slightly increasing to 15.32 mm at $k = 5$.

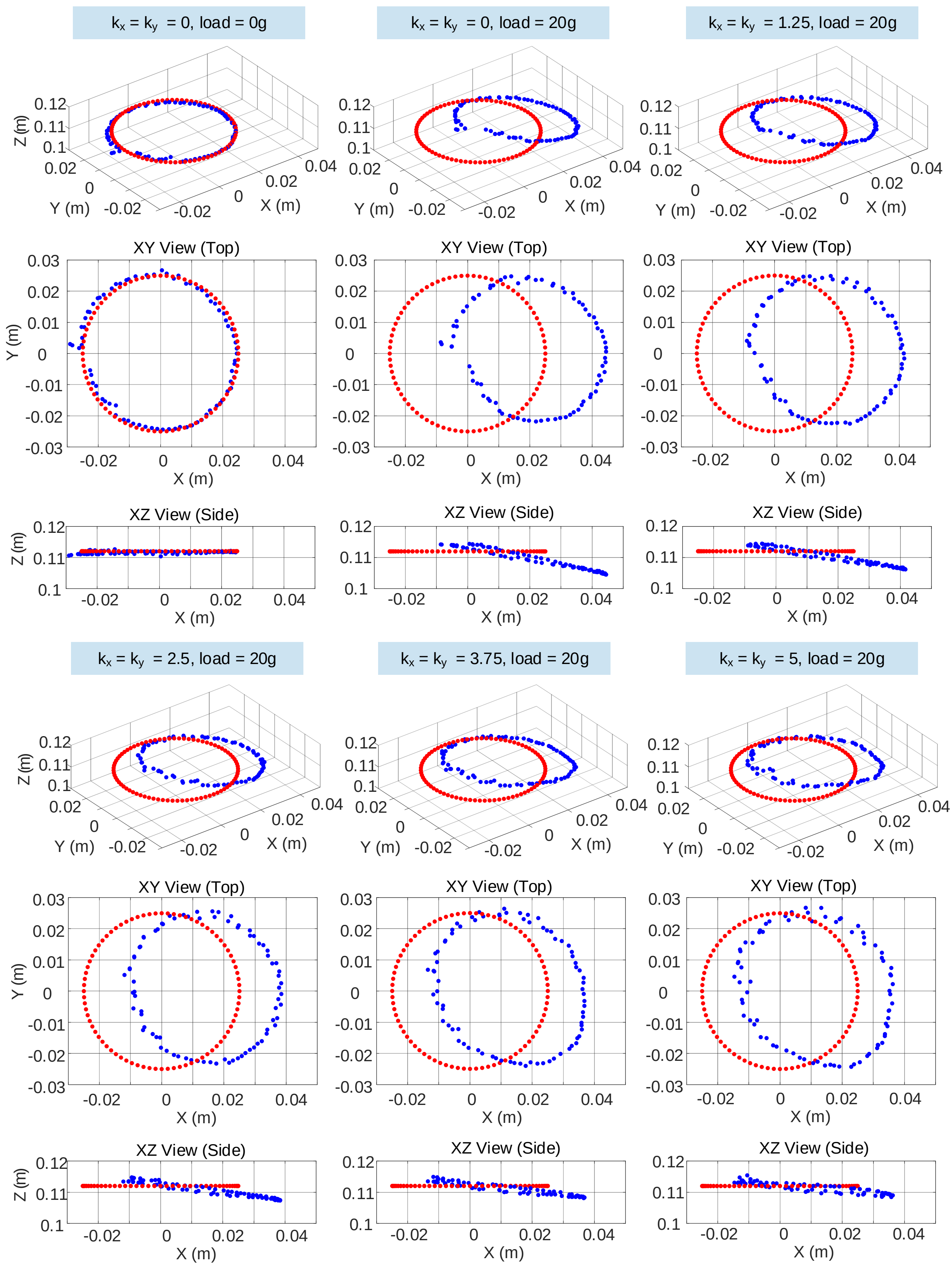

Figure 31: Circular trajectory holding performance under different in-plane stiffness gains $k_x = k_y = 0,\ 1.25,\ 2.5,\ 3.75,\ 5$ *with a* $20\,\mathrm{g}$ *external load, shown in 3D, top, and side views.*

To evaluate the statistical significance of these improvements, pairwise Welch's t-tests were

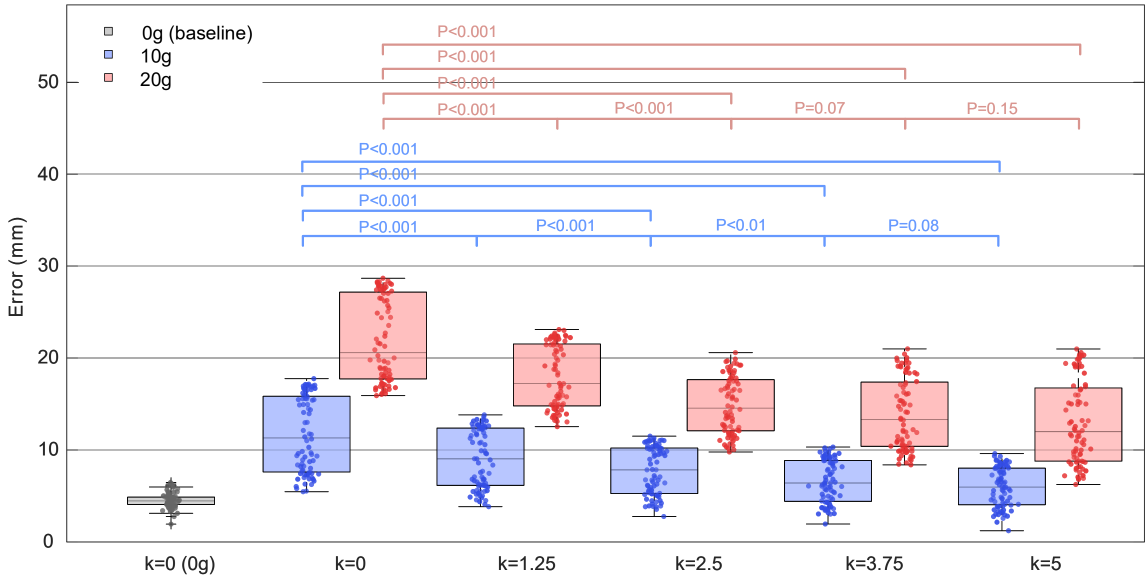

Figure 32: Tracking error for circular trajectory holding under different in-plane stiffness gains $k_x = k_y = 0,\ 1.25,\ 2.5,\ 3.75,\ 5$ with external loads of $0\,$g (baseline), $10\,$g, and $20\,$g.

performed across different stiffness gains under each loading condition. For the $10\,$g load, most pairwise comparisons yielded highly significant differences ($p < 0.001$), confirming that increasing k substantially improves trajectory accuracy. For the $20\,$g load, the difference between $k = 0$ and $k = 3.75$ was highly significant ($p < 0.001$), while the improvement from $k = 3.75$ to $k = 5$ was not statistically significant ($p = 0.15$). These results demonstrate that larger stiffness gains effectively reduce trajectory error, but the benefit saturates beyond $k = 3.75$ under higher loading conditions.

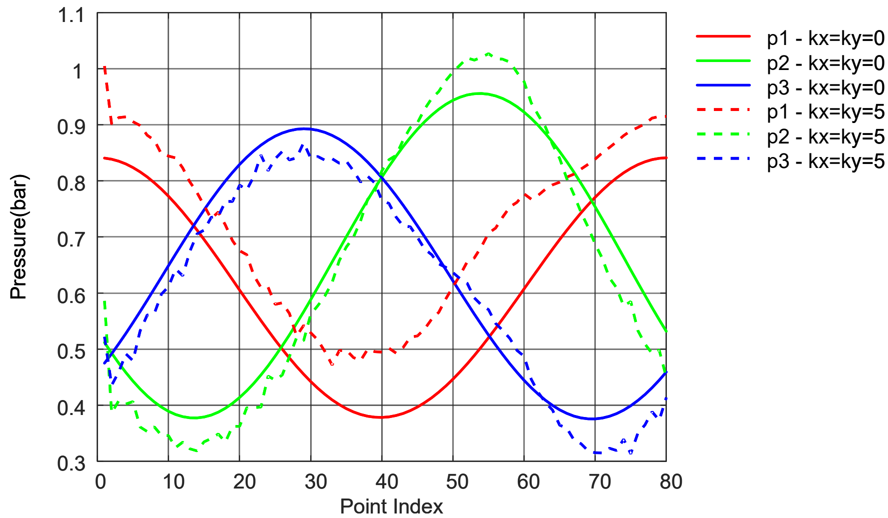

Figure 33: Chamber pressure profiles ($p_1,\ p_2,\ p_3$) during circular trajectory holding under different stiffness gains $k_x = k_y = 0$ and $k_x = k_y = 5$ with a $20\,$g external load.

Figure 33 shows the chamber pressure profiles (p_1, p_2, p_3) under a $20\,$g in-plane load for $k_x = k_y = 0$ and 5. Without regulation, all three pressures follow nearly sinusoidal patterns synchronised with the circular motion. With $k_x = k_y = 5$, p_1 shifts upward while p_2 and p_3 are also modulated but with smaller amplitude changes. At the endpoint located along the positive x-axis (index ≈ 40), p_1 increases from 0.37 bar to 0.50 bar. Around their respective peaks and valleys, p_2 and p_3 exhibit smaller modulations of about 0.07 bar.

Results of circular trajectory holding with vertical loading. Figure 34 illustrates the measured circular trajectories under a constant vertical load of 20 g for three stiffness settings, i.e., $k_z \in \{0, 10, 20\}$, compared against the unloaded baseline ($k_z = 0$, $load = 0$ g). When $k_z = 0$, the applied vertical load caused a visible downward shift of the entire trajectory in the z-direction and a radial contraction in the x–y plane. Increasing k_z effectively keeps measured trajectories closer to the desired circular path and results in less vertical sagging.

The RMSE values over the full trajectory are summarised in Figure 35. From $k_z = 0$ to $k_z = 20$, the RMSE decreased from 9.19 mm to 7.30 mm, corresponding to a 21 % reduction. At the intermediate setting of $k_z = 10$, the RMSE was 8.02 mm. To assess statistical significance, pairwise Welch's *t*-tests were conducted across different stiffness settings. The reduction in RMSE from $k_z = 0$ to $k_z = 20$ was statistically significant ($p < 0.05$), whereas the differences between $k_z = 0$ and $k_z = 10$ ($p = 0.16$), as well as between $k_z = 10$ and $k_z = 20$ ($p = 0.44$), were not significant.

Figure 36 shows the chamber pressure profiles. Without regulation, the pressures exhibit nearly sinusoidal variations. With $k_z = 20$, the modulation is minor and mainly occurs around the peaks and valleys of each chamber, with a maximum change of 0.03 bar.

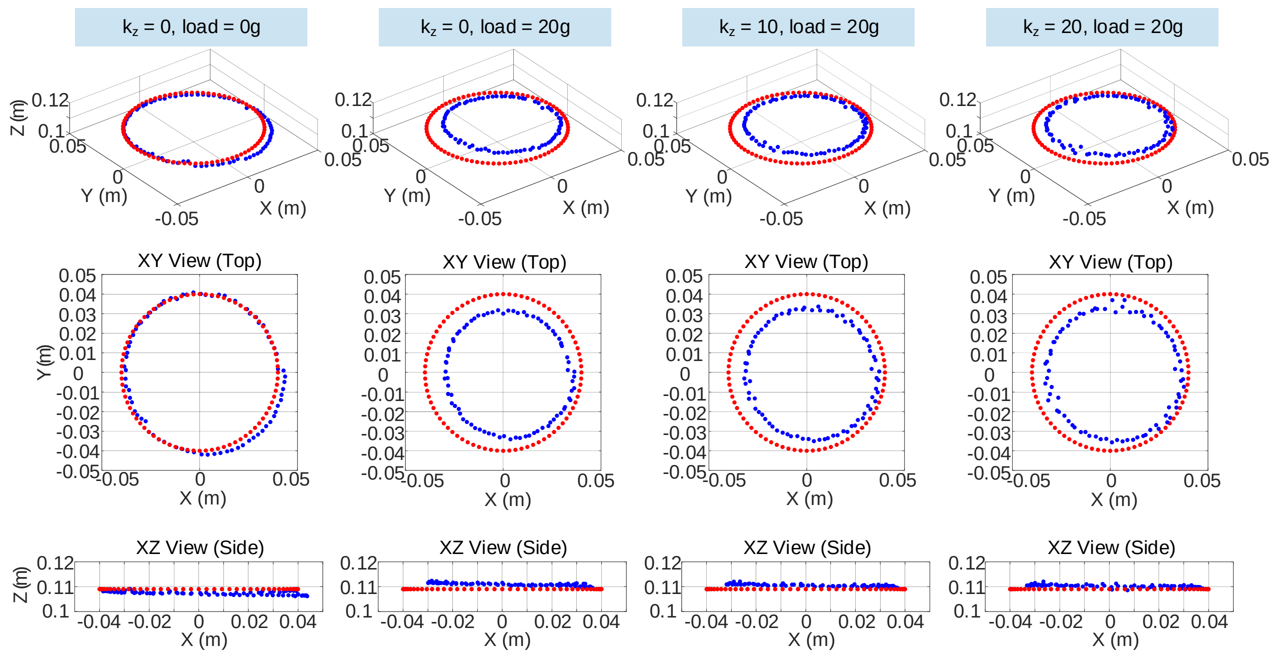

Figure 34: Circular trajectory holding performance under different vertical stiffness gains $k_z = 0,\ 10,\ 20$ with a 20 g vertical load, shown in 3D, top, and side views.

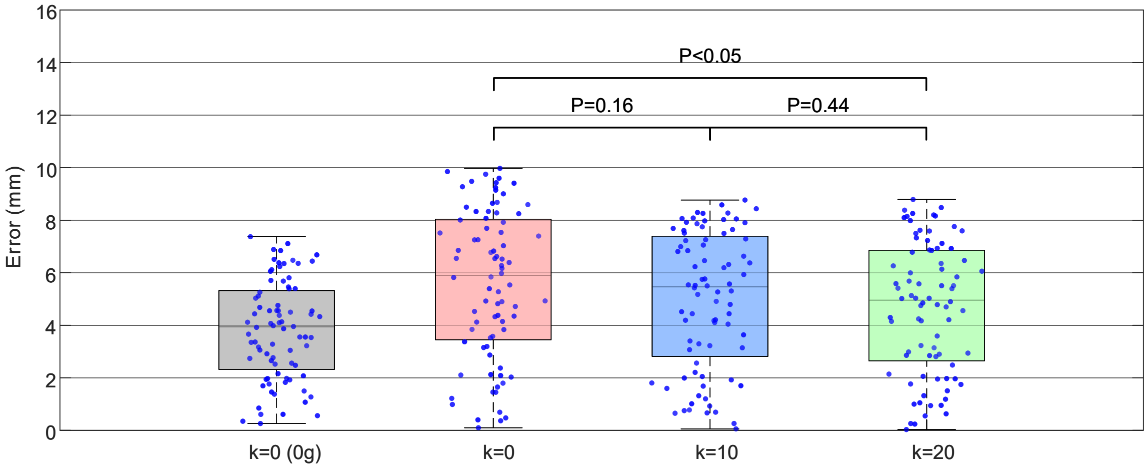

Figure 35: Tracking error for circular trajectory holding under different vertical stiffness gains $k_z = 0,\ 10,\ 20$ with a $20\,$g vertical load.

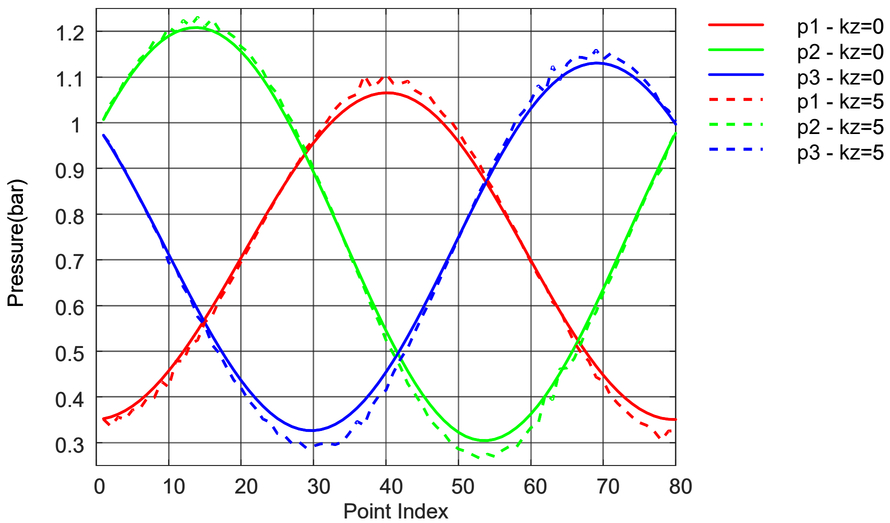

Figure 36: Chamber pressure profiles (p_1, p_2, p_3) during circular trajectory holding under different vertical stiffness gains $k_z = 0$ and $k_z = 20$ with a $20\,$g vertical load.

4.4.3 Position and Compliance-Softening Control for Obstacle Avoidance

This experiment evaluated the robot's ability to bypass obstacles by increasing robot compliance (softening control) during trajectory tracking.

Four trajectories were tested, including two planar paths in the x–y plane (a circular trajectory with a radius of $R_{\text{circle}} = 25\,$mm and a square trajectory with a side length of $L_{\text{square}} = 50\,$mm) and two spatial helical paths in 3D space (a cylindrical helix and a square helix) with a vertical rise of $\Delta z = 0.5\,$mm per revolution and $N_{\text{rev}} = 15$ turns. A cylindrical obstacle with a radius of $r_{\text{obs}} = 20\,$mm and a height of $h_{\text{obs}} = 35\,$mm was positioned so that the nominal paths entered its vicinity; the location was known beforehand for all experiments. At each trajectory point, the desired tip waypoint p^{ref} was sent to the inverse kinematics solver to compute the corresponding chamber pressures (p_1, p_2, p_3), which were applied to the pneumatic regulators in real time. Two control strategies were tested: (i) **No compliance regulation**, where the virtual stiffness gains were set to $k_x = k_y = 0$ along the entire path; (ii) **Region-based softening**, where negative stiffness gains ($k_x = k_y = -3$) were manually assigned to a predefined region around the obstacle to locally reduce stiffness along the x and y axes, while the rest of the trajectory was executed without compliance regulation ($k_x = k_y = 0$). During each run, the tip position was recorded using the Aurora electromagnetic tracking system, and the commanded chamber pressures were simultaneously logged.

Figure 37 presents the 2D obstacle-avoidance results. In Figure 37(a), the obstacle is initially at $(x = 0.04,\ y = 0.005)$ m and the nominal circular path (red) enters its region. Without compliance regulation ($k_x = k_y = 0$), the measured path (blue) stays close to the reference, so the robot's outer contour reconstructed from the centrally mounted sensor (green) intrudes into the obstacle region, indicating contact. The obstacle is consequently moved from its initial position to $(x = 0.048,\ y = 0.001)$ m, $(x = 0.050,\ y = 0.001)$ m, and $(x = 0.050,\ y = 0)$ m over repeated trials. By contrast, in Figure 37(b), *region-based softening* is used: negative gains ($k_x = k_y = -3$) are applied only at trajectory points 35–65 to locally reduce directional stiffness, while the rest of the path runs without regulation ($k_x = k_y = 0$). Under this mode, the path bends to follow the obstacle boundary in light sliding contact without penetration; the obstacle remains at its initial position. Outside the softening period, the trajectory closely follows the nominal circle.

Figures 37(c)-(d) report the square-trajectory case with the obstacle initially at $(x = 0.04,\ y = -0.002)$ m. Without compliance regulation ($k_x = k_y = 0$), the measured paths remain close to the nominal square, yet the reconstructed cross-sectional envelope intrudes into the obstacle region. The obstacle is consequently displaced to three nearby locations over repeated trials: $(x = 0.051,\ y = -0.017)$ m, $(x = 0.051,\ y = -0.016)$ m, and $(x = 0.052,\ y = -0.017)$ m. With *region-based softening* ($k_x = k_y = -3$ applied only at trajectory points 25–55 and $k_x = k_y = 0$ elsewhere), the path bends outward near the obstacle in light sliding contact without penetration; the obstacle remains at its initial position, and the trajectory adheres to the reference outside the softening region.

Figures 37(e)-(f) show the chamber pressure profiles (p_1, p_2, p_3) for the circular and square cases, respectively. In the baseline condition ($k_x = k_y = 0$, solid lines), the pressures follow the nominal pattern for path tracking. Within the softening region (points 35–65 for the circle; 25–55 for the square), p_1 (the pressure that drives bending away from the obstacle) increases, while p_2 (facing the obstacle) decreases; p_3 slightly increases. Outside the region, all three pressures revert to the nominal pattern and the trajectory adheres to the reference.

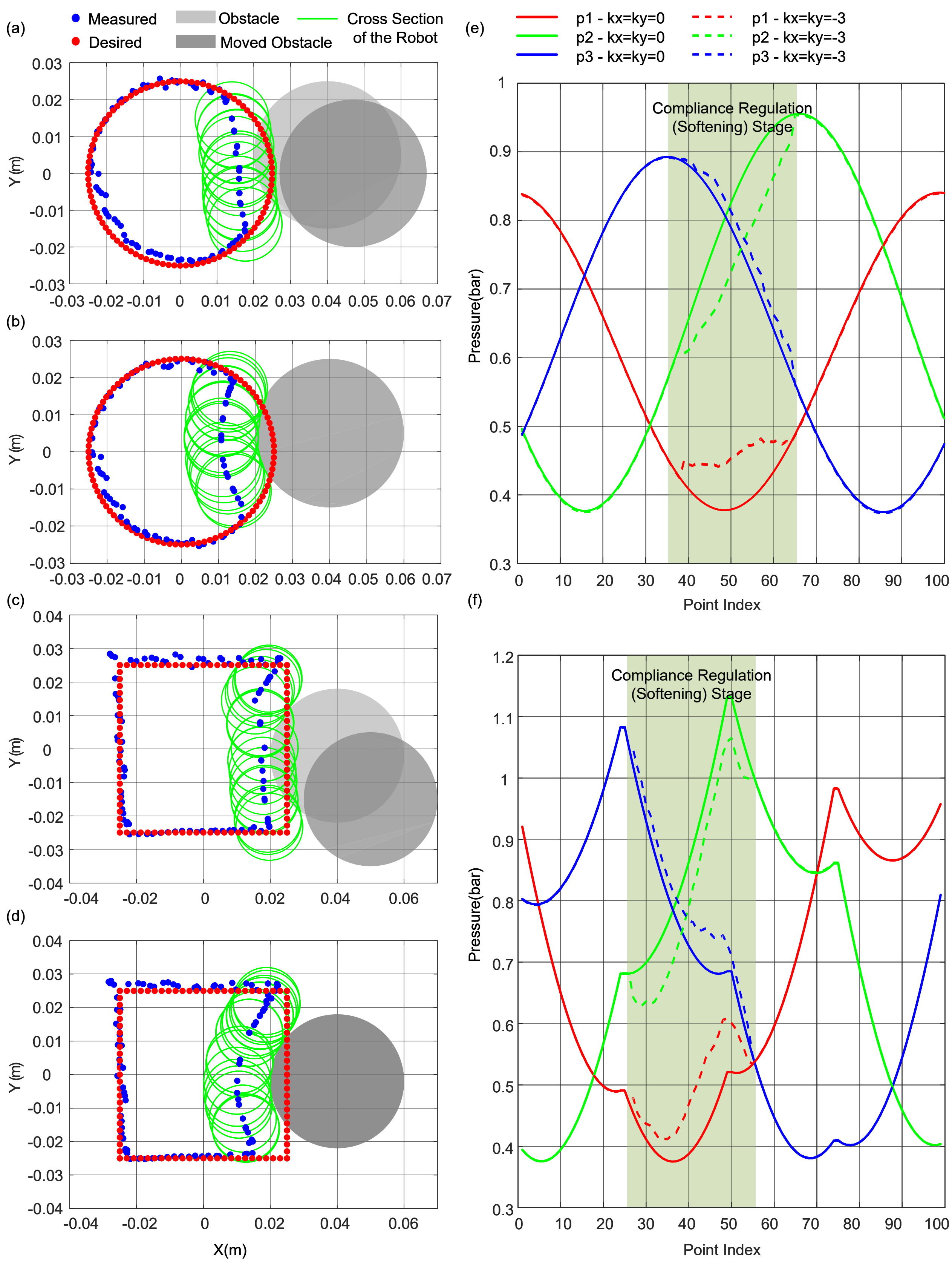

Figure 37: 2D obstacle avoidance performance. (a) Along the circular trajectory, without compliance regulation ($k_x = k_y = 0$). (b) Along the circular trajectory, with compliance regulation ($k_x = k_y = -3$). (c) Along the square trajectory, without compliance regulation ($k_x = k_y = 0$). (d) Along the square trajectory, with compliance regulation ($k_x = k_y = -3$). (e) Chamber pressure profiles (p_1, p_2, p_3) along the circular trajectory. (f) Chamber pressure profiles (p_1, p_2, p_3) along the square trajectory.

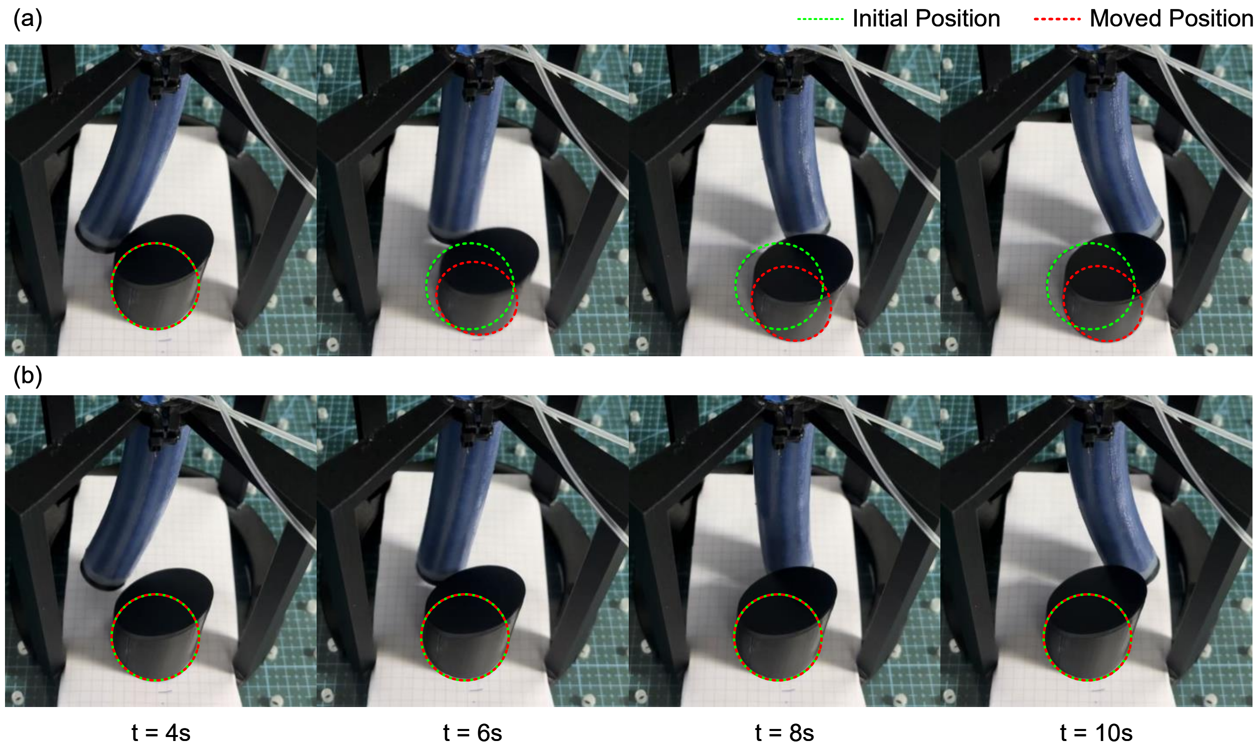

Figure 38: Snapshots of obstacle avoidance along the square path. (a) No compliance regulation ($k_x = k_y = 0$): contact displaces the obstacle. (b) Region-based softening ($k_x = k_y = -3$, points 25–55): the tip skirts the obstacle in light sliding contact; the obstacle remains at its initial position.

Figure 38 provides snapshots of the square-path experiment: without compliance regulation, the obstacle is displaced on contact, whereas with region-based softening ($k_x = k_y = -3$, points 25–55), the tip follows the obstacle boundary in light sliding contact and the obstacle doesn't move.

Figure 39 shows the 3D obstacle avoidance results for the cylindrical helix. In Figure 39(a), the obstacle is at $(x = 0.04,\ y = 0.005)$ m and partially overlaps with the desired trajectory. Without compliance regulation, the measured path (blue) stays close to the reference, so the robot's outer cross-sectional envelope (green) penetrates the obstacle volume and repeated contacts occur. The obstacle is pushed away to three nearby locations over repeated runs: $(x = 0.049,\ y = 0.001)$ m, $(x = 0.048,\ y = 0)$ m, and $(x = 0.051,\ y = 0)$ m. By contrast, in Figure 39(b) a region-based softening is used: negative gains ($k_x = k_y = -3$) are applied only within a predefined region around the obstacle and $k_x = k_y = 0$ elsewhere. Under this mode, the path deflects outward and follows the obstacle boundary in light sliding contact without penetration; after clearing the obstacle, it returns to the desired trajectory.

Figure 39(c) shows the corresponding chamber pressure (p_1, p_2, p_3) for the cylindrical spiral trajectory. In the baseline case ($k_x = k_y = 0$), the pressures follow the nominal periodic pattern required for spiral motion. When compliance regulation is activated within the highlighted softening region, the chamber pressures facing the obstacle (p_2) are dynamically reduced,

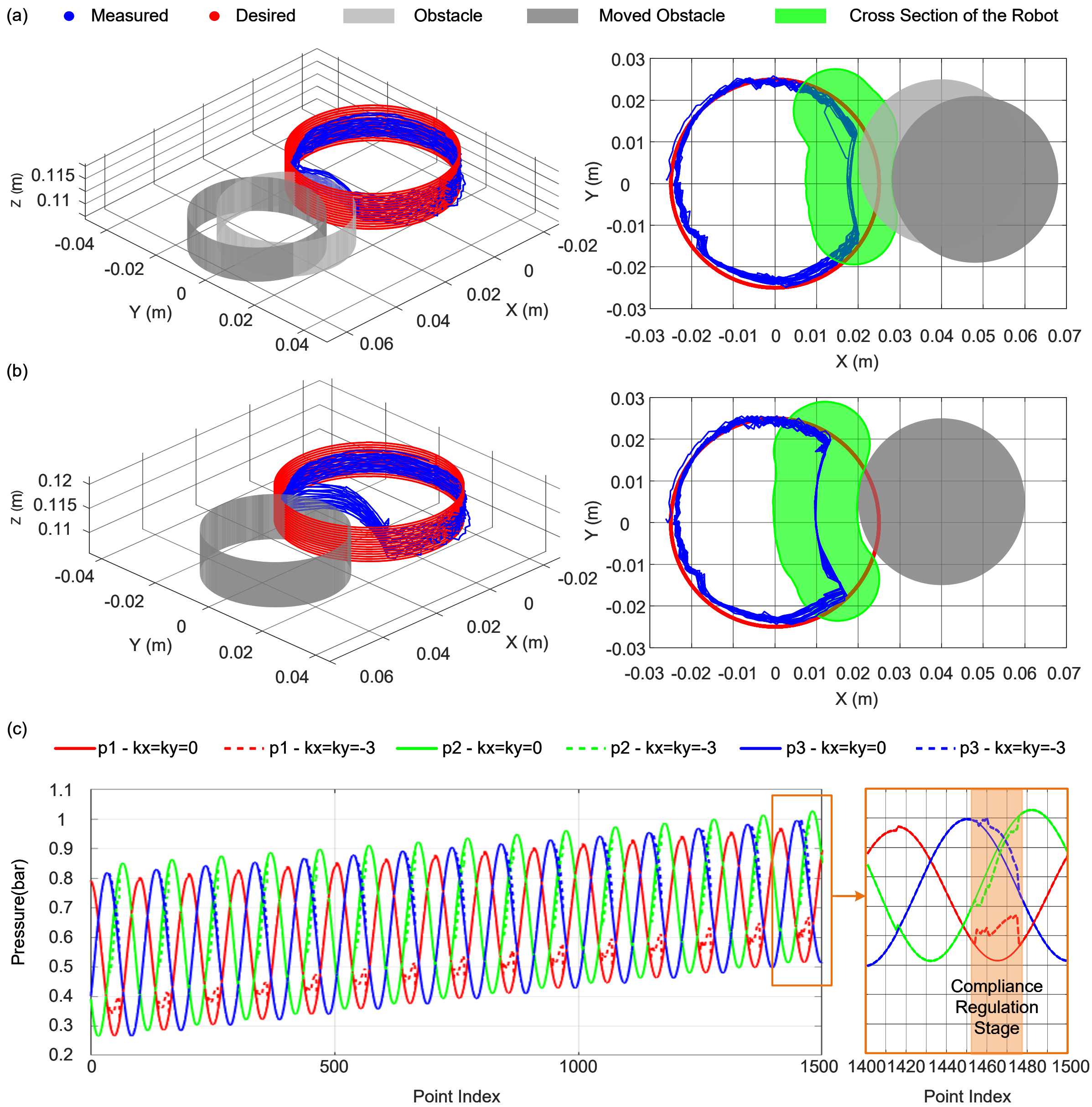

Figure 39: 3D obstacle avoidance performance along the cylindrical helix trajectory. (a) Without compliance regulation ($k_x = k_y = 0$). (b) With compliance regulation ($k_x = k_y = -3$). (c) Chamber pressure profiles (p_1, p_2, p_3).

while the opposite chambers (p_1) increase accordingly. This coordinated redistribution of chamber pressures reduces robot's stiffness, enabling smooth deformation of the robot tip around the obstacle boundary.

Similarly, Figure 40 presents the results for the square helix trajectory. In Figure 40(a), the obstacle is placed at $(x = 0.04, y = -0.002)$ m, and the desired square spiral trajectory (red) intersects the obstacle region. Without compliance regulation, the measured trajectories closely follow the desired square helix, causing the robot's cross-sections to penetrate the obstacle volume, especially along the edge segments, which leads to repeated collisions and displaces the obstacle to three nearby locations: $(x = 0.051, y = -0.018)$ m, $(x = 0.050, y = -0.017,)$ m, and $(x = 0.053, y = -0.018,)$ m. With compliance regulation, as shown in Figure 40(b), the trajectory bends outward in the vicinity of the obstacle, adapting to its outer contour in 3D space. After bypassing the obstacle, the trajectory recovers to the desired square spiral trajectory.

Figure 40(c) shows the corresponding chamber pressure profiles (p_1, p_2, p_3) for the square spiral trajectory. Similarly to the cylindrical case, the baseline pressures ($k_x = k_y = 0$) follow the nominal periodic pattern, while compliance regulation results in reduced pressures in the chambers facing the obstacle and compensatory increases in the opposite chambers, thereby reducing local stiffness and enabling adaptive obstacle avoidance.

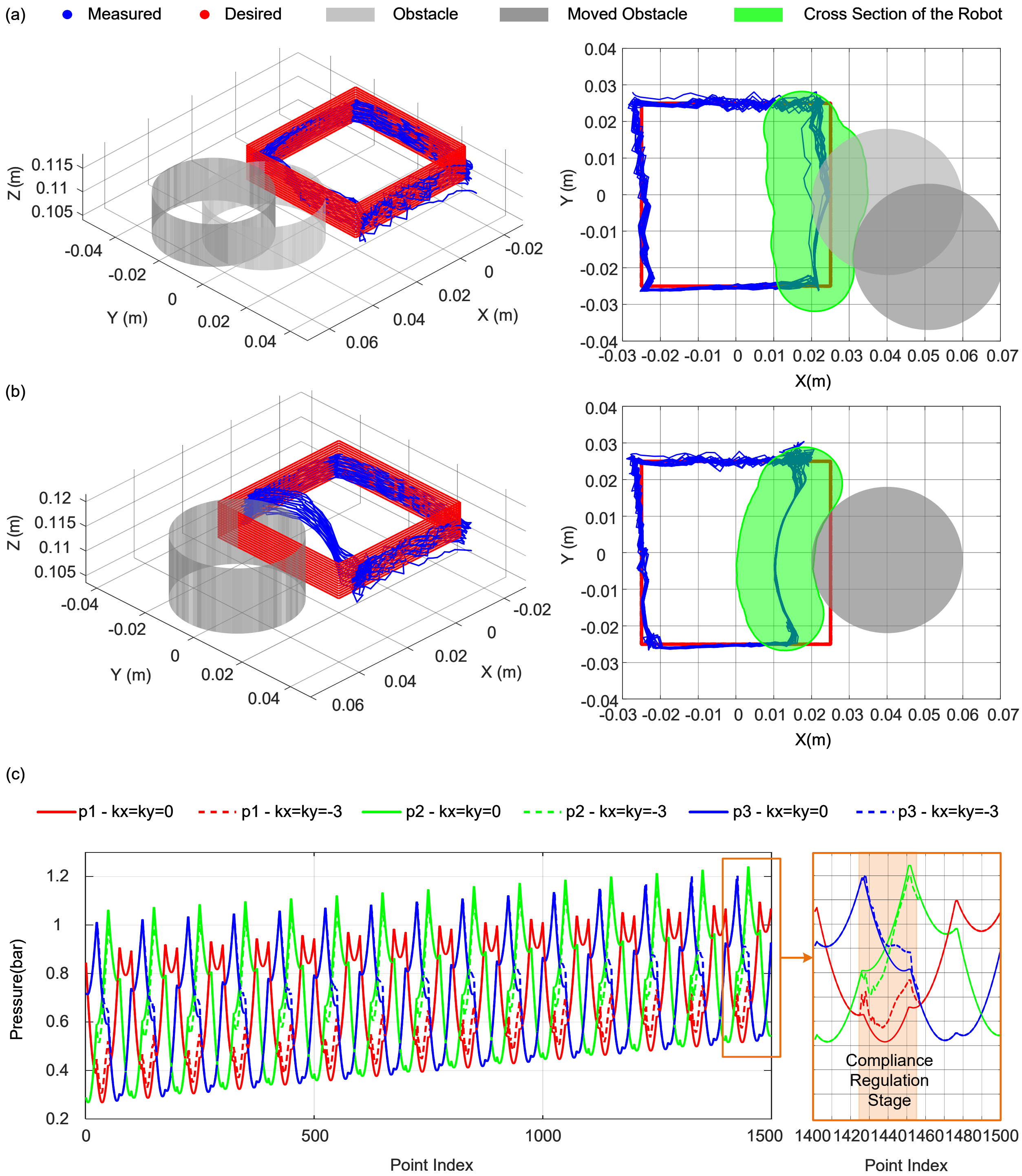

Figure 40: 3D obstacle avoidance performance along the square helix trajectory. (a) Without compliance regulation ($k_x = k_y = 0$). (b) With compliance regulation ($k_x = k_y = -3$). (c) Chamber pressure profiles (p_1, p_2, p_3).

5 Discussion

5.1 Discussion of Parameter Identification

The parameter identification and cross-validation experiments presented in Section 4.2 demonstrate that incorporating the pressure-dependent Young's modulus $E(p)$ into the Cosserat rod model substantially improves the accuracy of kinematic predictions. The identified $E(p)$ effectively captures the nonlinear softening behaviour of the silicone material, allowing the model to accurately predict the deformation of the soft continuum robot under different actuation conditions.

From the bending experiments, it can be observed that the final model slightly overestimates the bending angle under single-chamber actuation (see Figure 18(a)), but matches the experimental results well under dual-chamber actuation. This is because the selected $E(p)$ curve was slightly biased toward the dual-chamber data during fitting. Given that most control tasks involve dual- or multi-chamber actuation, the resulting prediction accuracy meets the requirements for reliable performance in practical applications.

Cross-validation on the square and heart trajectories further confirms the robustness of the calibrated model. After incorporating $E(p)$, the predicted tip positions show good agreement with the experimental measurements, and the tracking performance remains consistent across different trajectories. During the experiments, small pointwise fluctuations were observed around the desired trajectories, whereas the computed chamber-pressure profiles remained smooth. These fluctuations are mainly caused by the dynamics of the pneumatic actuation system, such as valve response delays and small pressure ripples in the air supply, rather than deficiencies of the kinematic model.

Despite the overall high accuracy, small systematic discrepancies between prediction and measurement remain. These can be mainly attributed to four factors: (1) tracking sensor bias and noise, where residual offsets and drift in the Aurora system can introduce global errors in tip position; (2) material modulus fitting strategy, as the selected $E(p)$ curve is slightly biased toward dual-chamber data, leading to small overestimations under single-chamber actuation; (3) unmodelled viscoelasticity, which is negligible under quasi-static conditions but may become relevant in faster or time-varying loading; and (4) manufacturing tolerances, including minor variations in chamber radius, spacing, or wall thickness.

Overall, integrating the experimentally identified $E(p)$ within the Cosserat rod framework establishes a reliable forward kinematics model. Its high consistency under dual- and multi-chamber actuation ensures predictive accuracy in practical control scenarios. This improved model accuracy provides a solid foundation for the compliance regulation strategies discussed in the following chapters.

5.2 Discussion of Compliance Regulation Validation

The validation experiments in Section 4.3 demonstrate that the proposed compliance regulation strategy effectively modulates the equivalent stiffness of the soft continuum robot. This section discusses the observed control behaviours and additional findings derived from the results.

The experiments reveal a clear monotonic relationship between the virtual stiffness gain factors (k_x, k_y, k_z) and the measured tip deflection under fixed external loads. Higher gains reduce deflection, indicating increased equivalent stiffness, while lower gains lead to softer responses. These results confirm that directional compliance can be reliably regulated through gain adjustment, and the trends remain consistent across repeated trials.

A notable directional compliance difference was observed. Larger values of k_z are required to achieve a comparable level of compliance regulation along the z-axis than along the x/y directions. This indicates that the soft robot used in this project possesses higher inherent stiffness in the vertical direction, while its lateral stiffness is relatively lower. This difference is likely related to the chamber geometry, wall thickness, and material properties.

In addition, the chamber-pressure profiles indicate that higher gains lead to increased instability throughout the entire regulation process. These fluctuations are mainly attributed to solver sensitivity under high-gain conditions, as the inverse solver operates in a steeper optimisation space where the computed pressure commands become more sensitive to initialization, step size, and convergence criteria.

In summary, the compliance validation experiments show that: (1) directional compliance can be modulated reliably and monotonically through gain adjustment; (2) the z-axis exhibits higher inherent stiffness and a wider regulation range than the x/y directions; and (3) at high gains, small chamber-pressure oscillations occur throughout the regulation phase due to solver sensitivity.

5.3 Discussion of Application of Compliance Regulation

The three applications in Section 4.4 (active interaction control, position and compliance-stiffening control for trajectory holding, position and compliance-softening control for obstacle avoidance) demonstrate the significance of compliance regulation in different interaction scenarios. By adjusting the stiffness gains k, the system can dynamically balance the compliance response and the disturbance rejection. In particular, the trajectory holding and obstacle avoidance tasks further highlight the capability of position–stiffness co-regulation, where both endpoint accuracy and directional compliance are simultaneously controlled.

First, the robot-human interaction control experiment examined the active compliance regulation under hand-applied perturbations. Applying a positive stiffness gain on a single Cartesian axis produced counteracting chamber-pressure responses on that axis.

Second, the trajectory holding task under external loading represents a typical application of stiffness enhancement through position–stiffness co-regulation. When maintaining high-accuracy trajectory tracking, the system actively increases stiffness along the loading direction to suppress tip deflections caused by external disturbance. Moderate gains provide substantial improvements in tracking accuracy. However, excessively high gains lead to pronounced oscillations in chamber-pressure profiles and tip motion throughout the control process. These instabilities mainly arise from the inverse solver's increased sensitivity in steeper optimisation spaces. This suggests that high-stiffness control requires particular attention to numerical robustness, which may be improved through strategies such as warm-start initialisation, adaptive step sizing, or refined convergence criteria.

Finally, the obstacle avoidance experiments demonstrate the complementary role of position-stiffness co-regulation. To navigate constrained spaces, the controller reduces stiffness in the obstacle-facing direction via negative gains, allowing the robot to conform around obstacles while maintaining path fidelity. As shown in Figure 41, relative to full-path softening, the region-gated softening used in this project (negative gains limited to the contact region) yields smaller nominal-to-measured trajectory error outside contact and allows chamber pressures to revert to their nominal profiles. The reason is that tracking error is not zero, always-on softening continually converts that residual error into an additive pressure term, biasing pressures away from the nominal profile and reducing effective stiffness, which enlarges trajectory deviation. Restricting softening to the contact region removes this bias, restores stiffness, and lets the trajectory rejoin the reference path. By contrast, the unregulated baseline tended to displace the obstacle. These results highlight the value of on-demand compliance for safe, adaptive interaction in constrained environments.

In summary, the three application studies reveal several key findings: (1) On-demand compliance regulation along desired directions: The controller can independently regulate stiffness along individual axes in 3D space. (2) Hybrid position–compliance control: By coordinating position tracking with compliance modulation, the controller can achieve both stiffening (e.g., trajectory holding) and softening (e.g., obstacle avoidance) depending on task demands.

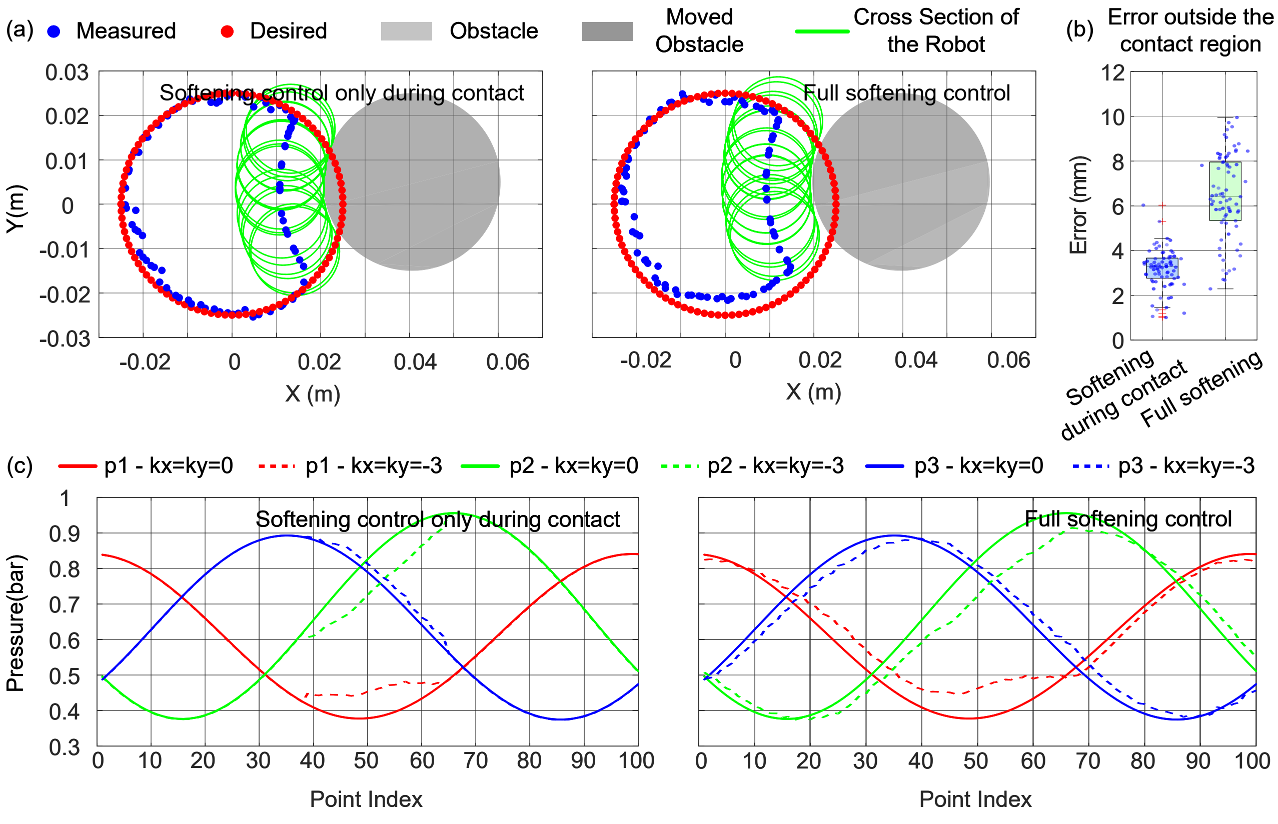

Figure 41: Comparison of 2D obstacle avoidance along a circular trajectory under two softening strategies. (a) Measured (blue) and desired (red) trajectories with the obstacle in gray: softening applied only during contact (left) and full softening (right). (b) Tracking error outside the contact region. (c) Chamber pressure profiles (p_1, p_2, p_3) for the two strategies.

(3) Stability constraints: High gains introduce solver sensitivity and numerical instabilities, requiring careful tuning and solver optimisation.

6 Conclusions

This thesis developed and validated a model–based framework for compliance regulation of a pneumatic–driven soft continuum robot. The approach integrates a quasi-static forward model based on the Cosserat-rod theory, a non-linear inverse kinematics solver, and a configuration–dependent compliance model, enabling position–stiffness co–regulation with minimal sensing and without auxiliary mechanical stiffening. A MATLAB front end with an optimised C++ MEX core supports real-time computation (1000 Hz) and practical experimentation.

On modelling and identification, a pressure–modulus law $E(p)$ was identified from bending calibration and embedded in the Cosserat-rod forward model, improving trajectory prediction accuracy on the calibration task. Cross-validation on unseen paths (a square and a heart curve, uniformly sampled) showed comparable accuracy to the calibration case, indicating out-of-sample generalisation.

With a configuration-dependent compliance map (from a local linearisation of the static equilibrium), the controller provides directional and monotonic stiffness regulation along the principal axes.In practice, the lateral axes permit wider softening–stiffening ranges, while the vertical axis requires larger gains to achieve the same effect due to higher inherent stiffness. These properties allow selective softening for safe interaction or stiffening for disturbance rejection as tasks demand.

The proposed controller was demonstrated across three application scenarios. For hand interaction, applying positive gains produced resisting responses to manual perturbations along all three axes. For trajectory holding, under external force loading along the x, y, or z axes, increasing the stiffness gain on the corresponding axis resulting in reduced trajectory deviations. For the obstacle avoidance, assigning negative gains on the obstacle-facing side softened the approach and allowed the robot to conform around nearby objects rather than pushing them away, thereby reducing interference during navigation in confined spaces. Overall, the results show practical benefits, including reduced trajectory deviation under external loads and reduced interference near obstacles.

Several limitations were observed. High gains increased solver sensitivity and could induce small oscillations, indicating the need for stronger numerical regularisation and more conservative step-size control. Residual model mismatch arises from sensor bias, manufacturing tolerances, and unmodelled viscoelastic effects at higher rates. Addressing these factors will further stabilise high-stiffness operation and improve generality across configurations.

In summary, this work provides a validated pipeline for soft-robot compliance regulation that couples accurate quasi-static modelling, efficient computation, and experimentally verified performance.

Future work will focus on: (1) exploring compliance regulation for multi-segment robots, (2) extending the material law to include rate-dependent viscoelasticity with online parameter adaptation; and (3) moving from quasi-static to dynamic scenarios, that co-optimises motion and stiffness during contact with improved control stability. These developments would broaden applicability to cluttered, uncertain environments and advance safe, high-performance manipulation with soft continuum robots.

References

Alici G & Shirinzadeh B (2005) Enhanced stiffness modeling, identification and characterization for robot manipulators. *IEEE Transactions on Robotics*, volume 21(4), pages 554–564.

Aloi V, Black C & Rucker C (2018) Stiffness control of parallel continuum robots. In *Dynamic Systems and Control Conference*, volume 51890, page V001T04A012. American Society of Mechanical Engineers.

Althoefer K (2018) Antagonistic actuation and stiffness control in soft inflatable robots. *Nature Reviews Materials*, volume 3(6), pages 76–77.

Babu SM, Sadeghi A, Mondini A & Mazzolai B (2019) Antagonistic pneumatic actuators with variable stiffness for soft robotic applications. In *2019 2nd IEEE International Conference on Soft Robotics (RoboSoft)*, pages 283–288. IEEE.

Black CB, Till J & Rucker DC (2017) Parallel continuum robots: Modeling, analysis, and actuation-based force sensing. *IEEE Transactions on Robotics*, volume 34(1), pages 29–47.

Camp AS, Chapman EM & Jaramillo Cienfuegos P (2021) Modeling and analysis of hydraulic piston actuation of mckibben fluidic artificial muscles for hand rehabilitation. *The International Journal of Robotics Research*, volume 40(1), pages 136–147.

De Pascali C, Naselli GA, Palagi S, Scharff RB & Mazzolai B (2022) 3d-printed biomimetic artificial muscles using soft actuators that contract and elongate. *Science Robotics*, volume 7(68), page eabn4155.

Della Santina C, Katzschmann RK, Bicchi A & Rus D (2020) Model-based dynamic feedback control of a planar soft robot: trajectory tracking and interaction with the environment. *The International Journal of Robotics Research*, volume 39(4), pages 490–513.

Gravagne IA & Walker ID (2002) Manipulability, force, and compliance analysis for planar continuum manipulators. *IEEE Transactions on Robotics and Automation*, volume 18(3), pages 263–273.

Huang X, Zhu X & Gu G (2022) Kinematic modeling and characterization of soft parallel robots. *IEEE Transactions on Robotics*, volume 38(6), pages 3792–3806.

Ilievski F, Mazzeo AD, Shepherd RF, Chen X & Whitesides GM (2011) Soft robotics for chemists. *Angewandte Chemie International Editiion*.

Khalil TA, Habib S, Seadby SG & Maged SA (2024) A structural optimization analysis of cable-driven soft manipulator. *International Journal of Advanced Robotic Systems*, volume 21(2), page 17298806241246886.

Komatsu M, Yaguchi T & Nakajima K (2021) Algebraic approach towards the exploitation of "softness": The input–output equation for morphological computation. *The International Journal of Robotics Research*, volume 40(1), pages 99–118.

Lai J, Lu B & Chu HK (2021) Variable-stiffness control of a dual-segment soft robot using depth vision. *IEEE/ASME Transactions on Mechatronics*, volume 27(2), pages 1034–1045.

Liu M, Hao L, Zhang W & Zhao Z (2020) A novel design of shape-memory alloy-based soft robotic gripper with variable stiffness. *International Journal of Advanced Robotic Systems*, volume 17(1), page 1729881420907813.

Loeve AJ, van de Ven OS, Vogel JG, Breedveld P & Dankelman J (2010) Vacuum packed particles as flexible endoscope guides with controllable rigidity. *Granular Matter*, volume 12, pages 543–554.

Mahvash M & Dupont PE (2011) Stiffness control of surgical continuum manipulators. *IEEE Transactions on Robotics*, volume 27(2), pages 334–345.

McMahan W, Chitrakaran V, Csencsits M, Dawson D, Walker ID, Jones BA, Pritts M, Dienno D, Grissom M & Rahn CD (2006) Field trials and testing of the octarm continuum manipulator. In *Proceedings 2006 IEEE International Conference on Robotics and Automation, 2006. ICRA 2006.*, pages 2336–2341. IEEE.

Naselli GA & Mazzolai B (2021) The softness distribution index: towards the creation of guidelines for the modeling of soft-bodied robots. *The International Journal of Robotics Research*, volume 40(1), pages 197–223.

Navas E, Fernández R, Sepúlveda D, Armada M & Gonzalez-de Santos P (2021) Soft gripper for robotic harvesting in precision agriculture applications. In *2021 IEEE International Conference on Autonomous Robot Systems and Competitions (ICARSC)*, pages 167–172. IEEE.

Nwafor C, Laurent GJ & Rabenorosoa K (2023) Miniature parallel continuum robot made of glass: Analysis, design, and proof-of-concept. *IEEE/ASME Transactions on Mechatronics*, volume 28(4), pages 2038–2046.

Peters J, Nolan E, Wiese M, Miodownik M, Spurgeon S, Arezzo A, Raatz A & Wurdemann HA (2019) Actuation and stiffening in fluid-driven soft robots using low-melting-point material. In *2019 IEEE/RSJ International Conference on Intelligent Robots and Systems (IROS)*, pages 4692–4698. IEEE.

Rucker DC & Webster RJ (2011) Computing jacobians and compliance matrices for externally loaded continuum robots. In *2011 IEEE International Conference on Robotics and Automation*, pages 945–950. IEEE.

Runciman M, Darzi A & Mylonas GP (2019) Soft robotics in minimally invasive surgery. *Soft robotics*, volume 6(4), pages 423–443.

Rus D & Tolley MT (2015) Design, fabrication and control of soft robots. *Nature*, volume 521(7553), pages 467–475.

Shi J, Shariati A, Abad SA, Liu Y, Dai JS & Wurdemann HA (2024) Stiffness modelling and analysis of soft fluidic-driven robots using lie theory. *The International Journal of Robotics Research*, volume 43(3), pages 354–384.

Spong MW, Hutchinson S & Vidyasagar M (2020) *Robot modeling and control*. John Wiley & Sons.

Stella F, Hughes J, Rus D & Della Santina C (2023) Prescribing cartesian stiffness of soft robots by co-optimization of shape and segment-level stiffness. *Soft Robotics*, volume 10(4), pages 701–712.

Stilli A, Kolokotronis E, Fraś J, Ataka A, Althoefer K & Wurdemann HA (2018) Static kinematics for an antagonistically actuated robot based on a beam-mechanics-based model. In *2018 IEEE/RSJ International Conference on Intelligent Robots and Systems (IROS)*, pages 6959–6964. IEEE.

Wehner M, Truby RL, Fitzgerald DJ, Mosadegh B, Whitesides GM, Lewis JA & Wood RJ (2016) An integrated design and fabrication strategy for entirely soft, autonomous robots. *Nature*, volume 536(7617), pages 451–455.

Wei Y, Chen Y, Ren T, Chen Q, Yan C, Yang Y & Li Y (2016a) A novel, variable stiffness robotic gripper based on integrated soft actuating and particle jamming. *Soft Robotics*, volume 3(3), pages 134–143.

Wei Y, Chen Y, Yang Y & Li Y (2016b) A soft robotic spine with tunable stiffness based on integrated ball joint and particle jamming. *Mechatronics*, volume 33, pages 84–92.

Yang C, Kang R, Branson DT, Chen L & Dai JS (2019) Kinematics and statics of eccentric soft bending actuators with external payloads. *Mechanism and Machine Theory*, volume 139, pages 526–541.

Yang Y, Zhang Y, Kan Z, Zeng J & Wang MY (2020) Hybrid jamming for bioinspired soft robotic fingers. *Soft Robotics*, volume 7(3), pages 292–308.

Yoshida S, Morimoto Y, Zheng L, Onoe H & Takeuchi S (2018) Multipoint bending and shape retention of a pneumatic bending actuator by a variable stiffness endoskeleton. *Soft Robotics*, volume 5(6), pages 718–725.

Zhao W, Zhang Y & Wang N (2021) Soft robotics: Research, challenges, and prospects. *Journal of Robotics and Mechatronics*, volume 33(1), pages 45–68.

Zhu M, Mori Y, Wakayama T, Wada A & Kawamura S (2019) A fully multi-material three-dimensional printed soft gripper with variable stiffness for robust grasping. *Soft Robotics*, volume 6(4), pages 507–519.

Appendix A: AI-Assisted Writing Declaration

During this project, I used ChatGPT to polish the language of the thesis.